UNIVERSIDADE FEDERAL DE PERNAMBUCO
DEPARTAMENTO DE FÍSICA – CCEN
PROGRAMA DE PÓS-GRADUAÇÃO EM FÍSICA

Edwin Danelli Coronel Sánchez

Optically detected magnetic resonance in nanodiamonds with single nitrogen-vacancy defects

Recife
2016

Edwin Danelli Coronel Sánchez

Optically detected magnetic resonance in nanodiamonds with single nitrogen-vacancy defects

Dissertação apresentada ao Programa de Pós-Graduação em Física do Departamento de Física da Universidade Federal de Pernambuco como parte dos requisitos para obtenção do título de Mestre em Física.

Supervisor:
Leonardo de Souza Menezes

Recife
2016

Catalogação na fonte
Bibliotecária Joana D'Arc Leão Salvador CRB 4-572

C822o Coronel Sánchez, Edwin Danelli.
Optically detected magnetic resonance in nanodiamonds with single nitrogen-vacancy defects / Edwin Danelli Coronel Sánchez . – 2016.
80 f.: fig.

Orientador: Leonardo de Souza Menezes.
Dissertação (Mestrado) – Universidade Federal de Pernambuco. CCEN. Física. Recife, 2016.
Inclui referências.

1. Óptica. 2. Ressonância magnética. 3. Espectroscopia de alta resolução. I. Menezes, Leonardo de Souza (Orientador). II. Titulo.

535.2 CDD (22. ed.) UFPE-FQ 2016-29

Edwin Danelli Coronel Sánchez

Optically detected magnetic resonance in nanodiamonds with single nitrogen-vacancy defects

Dissertação apresentada ao Programa de Pós-Graduação em Física do Departamento de Física da Universidade Federal de Pernambuco, como requisito parcial para a obtenção do título de Mestre em Física.

Aprovada em: 28/04/2016.

BANCA EXAMINADORA

Prof. Dr. Leonardo de Souza Menezes
Orientador
Universidade Federal de Pernambuco

Prof. Dr. Antonio Azevedo da Costa
Examinador Interno
Universidade Federal de Pernambuco

Prof. Dr. Marcos César Santos Oriá
Examinador Externo
Universidade Federal da Paraíba

This dissertation is dedicated to my parents Zacarias and Alicia. Thanks for giving me the best education that you could. I love you!

Acknowledgements

I would like to begin by thanking my supervisor Leonardo de Souza Menezes, for letting me be part of this project, for his teachings, his patience and confidence. Also, professor Whualkuer Lozano Bartra, who gave me the opportunity to work in his nonlinear optics laboratory. This fact certainly marked a important beginning in my professional life.

The professors of the Physics Department for their unconditional support and spending time in conversations about physics. Administrative staff, particularly Hilda and Alexsandra who are always supporting us in any urgent procedure we need. Daniel and Marcos of the electronics shop who always make available their expertise to fix our electronics apparatus.

I want to thank the people who are directly involved in the project: Professor Oliver Benson (Humboldt University Berlin) and his Ph.D. students Nikola Sadzak and Bernd Sontheimer, whose contributions were immensely important for the development of the project. Thanks Kelly and Bruno (Nano optics lab at UFPE) for supporting me in any issues arising in the laboratory.

Thanks all people who always help me when I need it: Albert, Milrian, Hugo, Lesli, Camilo, Fania, Jaiver, Oscar, Pablo, Alison. Special thanks for Marcos, Johana, Lenin, Winnie and Johan who over two years of study proved to be great friends. In particular Johan that shares a peculiar linking for physics like me.

For most important people in my life, my family and specially my parents, who sacrificed many things in their lifes to give me education, the time I'll live won't be enough to thank them. Thanks Rosario for being important in my life and always supporting me in my decisions.

« Nobody ever figures out what life is all about, and it doesn't matter. Explore the world. Nearly everything is really interesting if you go into it deeply enough »

Richard Feynman

Resumo

O controle da interação radiação-matéria, em nosso caso de fótons com emissores quânticos individuais, como os defeitos de nitrogênio-vacância (NV) em nanodiamantes, é crucial no processo da fabricação de nano-dispositivos. Isto é conseguido aproveitando-se os últimos avanços em nano-óptica para aumentar a interação com emissores únicos, para os quais ferramentas adequadas para o controle preciso da interação foi desenvolvido. Nesta dissertação, descreveremos o uso de um microscópio confocal invertido e manipulação coerente dos estados de spin de um defeito individual NV num nanodiamante. Os defeitos NV em nanodiamantes apresentam propriedades ópticas que dependem do estado de spin dos seus elétrons opticamente ativos, o que os tornam interessantes para aplicações em nanomagnetometria, processamento de informação quântica e nanobiotermometria. Em particular, defeitos NV negativamente carregados (NV^-) exibem emissão de fótons únicos e longos tempos de coerência, mesmo à temperatura ambiente. Além disso, têm um estado fundamental paramagnético e o sistema pode ser opticamente polarizado e lido, usando-se uma técnica experimental conhecida como Ressonância Magnética Detectada Opticamente (ODMR). Nesta técnica, a intensidade de fluorescência emitida pelo nanodiamante depende da configuração de spin do estado eletrônico fundamental, a partir do qual a transição eletrônica é excitada. Para estudar esses defeitos NV, nanodiamantes foram depositados ao longo de uma antena, fotolitograficamente estruturada sobre um coverslip, usando spin coating e colocados sobre o microscópio. O microscópio permite a detecção da fluorescência do defeito e sua excitação é feita por um laser CW emitindo em 532 nm. A fluorescência emitida pelo nanodiamante ocorre em torno dos 650 nm com uma linha zero fônon em 637 nm. A fluo-rescência coletada é enviada a dois fotodiodos de avalanche, que estão em configuração interferométrica do tipo Hanbury-Brown and Twiss (HBT). Nela, podemos garantir se a emissão coletada provém de um emissor individual, analisando a função de correlação de segunda ordem $g^{(2)}(\tau)$: se $g^{(2)}(\tau) < 0,5$ comprovamos a emissão de fótons únicos por um único defeito NV^- no nanodiamante. Trabalhamos então com um único defeito NV^- como emissor. Irradiando um campo de

microondas sobre o nanodiamante, nos permite determinar a frequência de ressonância com a transição de spin no estado fundamental, evidenciado por uma diminuição da fluorescência emitida pelo nanodiamante. Usamos o fato de que a frequência de ressonância da transição do spin depende do campo magnético local para observar o efeito Zeeman gerado pelo campo magnético de um ímã (Nd-Fe-B). Finalmente, realizamos manipulação coerente através de uma adequada sequência de pulsos de microondas e laser, observando oscilações de Rabi. Assim, pudemos medir o tempo de coerência inhomogêneo (T_2^*) dado pelo amortecimento das oscilações de Rabi.

Palavras Chave: Microscopia óptica confocal. Nanodiamantes. Fluorescência. Ressonância magnética. Dinâmica coerente.

Abstract

The control of the radiation-matter interaction, in our case of photons with quantum single emitters, as the nitrogen-vacancy (NV) defect in nanodiamonds, is crucial in the process of nano-devices fabrication. This is achieved taking advantage of the latest advances of the nano-optics to increase the interaction with single emitters for which ade-quate tools for precise interaction control has been developed. In this dissertation, we use a home-made inverted optical confocal microscope and coherent manipulation of spin states to study single NV defect in nanodiamonds. The NV defect in nanodiamonds presents optical properties that depend on the spin state of its optically active electrons, which makes them interesting for applications in nanomagnetometry, quantum information processing and nanobiothermometry. In particular, the negatively charged NV defect (NV^-) exhibits single photon emission and long coherence times even at room temperature. Furthermore, it has a paramagnetic ground state and can be optically polarized and read out, in an experimental technique known as Optically Detected Magnetic Resonance (ODMR). In this technique, the intensity of the fluorescence emitted by a nanodiamond depends on the spin configuration of the electronic ground state, from which an electronic transition is excited. In order to study these defects, nanodiamonds were deposited on a photolitographically structured antenna on a coverslip by spin coating and placed on the microscope. The microscope allows to both, the detection of the fluorescence and its excitation, by a CW laser emitting at 532 nm. The fluorescence emitted by the nanodiamond is centered around 650 nm with a zero phonon line at 637 nm. The collected fluorescence is sent to two avalanche photodiodes (APDs), that are in a configuration known as Hanbury-Brown and Twiss (HBT) interferometer. In it, we can verify whether the collected emission comes from an individual emitter, analyzing the second order correlation function $g^{(2)}(\tau)$: if $g^{(2)}(\tau) < 0.5$ we have an emission from single photons generated by a single NV^- defect in diamond. Working whit single emitter we could radiate a microwave field over the nanodiamond, which allows us to determine the resonance frequency for spin transitions in the ground state. At resonance one observes a drop in the fluorescence

emitted by the nanodiamond. We explore the fact that the resonance frequency of the spin transition depends on the local magnetic field to measure the Zeeman effect generated by the magnetic field of a permanent magnet (NdFeB). Finally, we realized coherent manipulation via an appropriate sequence of pulses of microwave and laser, observing Rabi oscillations. Thus, we can measure the inhomogeneous coherence time (T_2^*) given by the damping of Rabi oscillations.

Keywords: Confocal optical microscopy. Nanodiamond. Fluorescence. Magnetic resonance. Coherent dynamics.

List of Figures

Contents

Chapter 1

Introduction

Optically Detected Magnetic Resonance (ODMR) has been explored since the early 1970's when Breiland, Harris and Pines first demonstrated optical detection of electron precession and electron spin echoes by monitoring the phosphorecence of molecular excited triplet states [1]. ODMR has since then been used to study the polarization of nuclear spins in semiconductors and also for direct detection of local magnetic fields [2]. This technique also provides ultrasensitive means to detect and image a small number of electron and nuclear spins, down to the single spin level with nanoscale resolution [3]. Since a few years, this technique has being used in many applications and interesting physics has been revealed through the ODMR of nitrogen-vacancy (NV) defects in diamonds [4].

The study and characterization of defects have been of great importance for solid state physics and for development of technological devices because these defects frequently determine most of the mechanical, electrical and optical properties of solids [5, 6]. There is a class of defects that are optically active, called color centers [6]. The defects in diamonds are among many studied optically active defects [7], in particular the nitrogen-vacancy defects (NV). Two different forms of these defects have been identified to date, namely the neutral state NV^0 and the negatively charged state NV^-, and they have very different optical and spin resonance properties [8]. The advantages of these defects is that one is able to maintain their optical and quantum properties even working at ambient conditions. Probably, the NV defects are the best known solid state single photon source

operating at room temperature [9]. The electronic configuration of a NV^- defect leads to a spin system with $S = 1$ that can be optically detected as an individual quantum system and prepared in a defined quantum state by optical pumping.

Between the two types of defects (NV^0 and NV^-), the NV^- in nanodiamond is an important physical system that allows the development of many technologies including metrology [10], nanomagnetometry [11], nanothermometry [12] and quantum information processing [13].

Since diamond is a inert material, the crystalline matrix forms a shell around the defect that protects it, making that it has a weak coupling with the environment. This defect exhibits an efficient and perfectly photostable red photoluminiscence (PL), which enables easy optical detection of individual NV defects by confocal microscopy at room temperature. The extreme control in the production of pure diamond with nitrogen impurities permits that the NV^- spin states have exceptionally long coherence times in the order of 70 μs [14], which is very important for quantum information protocols. Moreover, NV^- can be optically addressed, and due to their spin dependent fluorescence, the electronic spin of a NV^- defect can be both initialized and read out with a simple optical setup. A full quantum coherence control can also be realized trough the application of microwave pulses on the optically initialized state with ODMR.

In this work, we present a study about the optical properties of single NV^- defects embedded in nanodiamonds using the ODMR technique. In chapter 2, we discuss the subject of photon statistics to classify the different types of light emitted and to introduce the concept of the second-order correlation function [$g^2(\tau)$] looking into the works of Hanbury-Brown and Twiss (HBT) [15, 16]. These are important concepts that will be essential in characterizing the detection of single photon emitters. Still in this chapter, we make a short review about coherent dynamics in a two level system where we introduce concepts such as Bloch vector and π pulses. Then, we describe the main properties of the NV defects and in particular the photophysics of the NV^- defect in diamond. Finally, we briefly describe the technique of optical confocal microscopy used, to study the nanodiamonds defects in our experiments.

In chapter 3, we describe our experimental apparatus and the way we get our samples: from the coverslip cleaning process passing through the description and use of the spin coating technique, until the way the microwave antennas used to perform the ODMR are fabricated. Then we show the detection of a single NV^- defect in a nanodiamond by means of HBT interferometry which is the first step to realize spin state manipulation using ODMR. Also the power broadening and the Zeeman splitting are shown. Furthermore the first measures of magnetometry and inhomogeneous dephasing time (T_2^*) via Rabi oscillations are realized.

Finally, in chapter 4 we present the conclusions and perspectives of our work.

Chapter 2

Theory and methods

In this chapter we develop theoretical aspects to set bases that will allow us to explain the results of this work. We begin by studying the quanta of the electromagnetic radiation, photons. We will study properties of the light from statistical and quantum (photon) perspectives. Light-matter interaction is another subject that we will review here, describing transient dynamics phenomena, particularly in a two level system for which we introduce the concept of optical Bloch equations. The experiments in this dissertation consist in investigating nanodiamonds with a single NV^- defect, thus we will also present concepts such as their structure and the photophysics of their emission. Finally, we will discuss about confocal microscopy that is a crucial method used for investigating single defects in nanodiamonds and that we apply in this work.

2.1 Photons

In this section, we study some basic concepts to understand the behavior of light. Our work uses coherent light as excitation source (a laser), so the description of the light properties done in this section is particularly to coherent light. First, we study different kinds of light and their characteristics classifying it according to the second-order correlation function $g^2(\tau)$, which allows to label light as bunched, coherent or antibunched. We emphasize here that the antibunching phenomenon is a signature of the quantum nature of light [17].

2.1.1 Coherent light and photon-counting statistics

One of the important things that we want to realize in our experiments is to determine if a particular nanodiamond contains a single defect, which is a source of single photons. In order to do that, to a given nanodiamond we need to count the number of photons emitted by it and that strike the detector in a specific time interval τ. We consider that the detected beam is perfectly coherent, monochromatic with an angular frequency ω and constant intensity I. According to the basic principles of classical electromagnetism, light is an electromagnetic wave. If the light is coherent with angular frequency ω, phase ϕ and amplitude E_0 the beam emitted by a laser can be represented by an electromagnetic field written as [18]

$$E(x,t) = E_0 \sin(kx - \omega t + \phi) \tag{2.1}$$

where $E(x,t)$ is the electric field of the light and $k = \omega/c$ is the wavenumber in free space.

In agreement with the quantum picture of light, the photon flux Φ is defined as the average number of photons passing through a cross-section of the beam in a unit time [19]. The photon flux is calculated dividing the power by the energy of the individual photons:

$$\Phi = \frac{IA}{\hbar\omega} = \frac{\mathcal{P}}{\hbar\omega} \text{ photons s}^{-1} \tag{2.2}$$

where A is the beam's cross section and $\mathcal{P}$ its power. The intensity I is proportional to the modulus square of the electromagnetic field amplitude and is constant only if E_0 and ϕ are independent of time. There will therefore be no intensity fluctuations and the average photon flux defined by the Equation 2.2 will be constant in the time. The quantum efficiency of the detector η gives us the ratio between the number of photocounts to the number of incident photons. To know the number of photons detected by the detector in a time τ we use the following expression

$$N(\tau) = \eta\Phi\tau = \frac{\eta\mathcal{P}\tau}{\hbar\omega} \tag{2.3}$$

where the average count rate $\mathcal{R}$ is given by

$$\mathcal{R} = \frac{N}{\tau} = \eta\Phi = \frac{\eta\mathcal{P}}{\hbar\omega} \tag{2.4}$$

The maximum count rate given by a detector is basically dependent on the detector deadtime, which is the time that is taken for the photon counting system to recover after one detection event. A beam of light with a given photon flux will present photon number fluctuations in a given time interval due to the discrete nature of the light, this being described by the photon statistics.

Coherent light follows the Poissonian photon statistics, that expresses the probability distribution of photon numbers as [19, 21]

$$P(n) = \frac{\overline{n}^n}{n!}\exp(-\overline{n}) \tag{2.5}$$

where $\overline{n}$ is the average number of events that are detected. In Figure 2.1 we show representative distributions for $\overline{n} = 0.1,\ 1.0,\ 5.0$ and 10.0, where one observes a broader distribution as $\overline{n}$ increases. The fluctuations of the statistical distribution around its mean value are quantified in terms of the variance. The variance is equal to the square of the standard deviation Δn and is defined by

$$Var(n) = (\Delta n)^2 = \sum_{n=1}^{\infty}(n-\overline{n})^2 P(n) \tag{2.6}$$

In the Poisson statistics, the variance is equal to the mean value $\overline{n}$ [19]:

$$(\Delta n)^2 = \overline{n} \tag{2.7}$$

So the standard deviation is given by

$$\Delta n = \sqrt{\overline{n}} \tag{2.8}$$

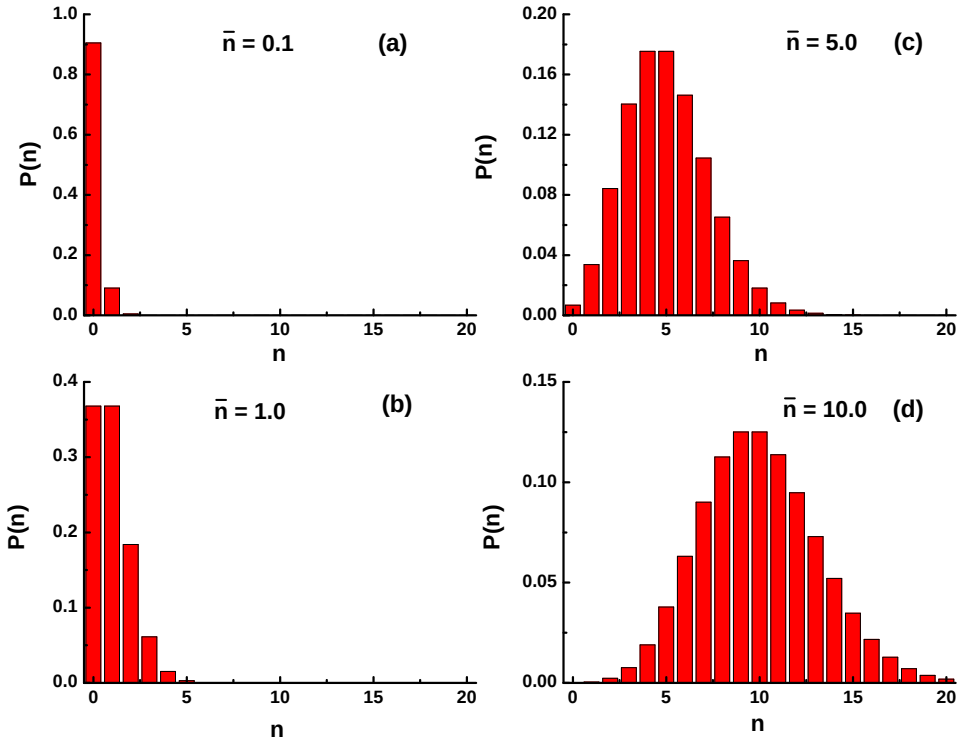

Figure 2.1: Behavior of the Poisson distribution for a light beam with constant intensity. The mean photon number $\overline{n}$ takes values 0.1 (a), 1.0 (b), 5.0 (c) and 10.0 (d).

The last equation shows that the relative size of the fluctuations $\Delta n/\overline{n}$ decreases as $\overline{n}$ gets larger. For example if $\overline{n} = 1.0$, we have $\Delta n = 1.0$ so that $\Delta n/\overline{n} = 1.0$. On the other hand, if $\overline{n} = 100.0$, we have $\Delta n = 10.0$, and $\Delta n/\overline{n} = 0.1$. Poissonian statistics is applied to random processes. We can say that although the average photon number has a fixed value, it fluctuates due to the discrete nature of the photons, when taking into account short time intervals. These fluctuations can give us useful information to identify different types of light, as will be seen at the end of this section.

Now we will consider the formalism of photon number representation taking into account the quantum theory of light based in the quantum harmonic oscillator formalism, which Hamiltonian is given by

$$\hat{H} = \hbar\omega\left(\hat{a}^{\dagger}\hat{a} + \frac{1}{2}\right) \tag{2.9}$$

where $\hat{a}^\dagger$ is the creation operator, for which:

$$\hat{a}^\dagger |n\rangle = (n+1)^{1/2} |n+1\rangle . \tag{2.10}$$

Similarly, to the annihilation operator $\hat{a}$ we have

$$\hat{a} |n\rangle = n^{1/2} |n-1\rangle \tag{2.11}$$

Furthermore, let $|n\rangle$ be an energy eigenstate of the Hamiltonian $\hat{H}$ with eigenvalues given by E_n in

$$\hat{H} |n\rangle = E_n |n\rangle = \left(n + \frac{1}{2}\right)\hbar\omega |n\rangle \tag{2.12}$$

To describe coherent states we use the Dirac notation. In this framework, a coherent state $|n\rangle$ is defined by [19, 22]:

$$|\alpha\rangle = exp(-|\alpha|^2/2) \sum_{n=0}^{\infty} \frac{\alpha^n}{(n!)^{1/2}} |n\rangle \tag{2.13}$$

where α is a dimensionless complex number and $|n\rangle$ is known as number (or Fock) state. Despite not being eigenstates of the Hamiltonian of the harmonic oscillator neither present orthogonality properties, the coherent states $|\alpha\rangle$ are eigenstates of the annihilation operator $\hat{a}$ with eingenvalue α:

$$\begin{aligned}
\hat{a} |\alpha\rangle &= exp(-|\alpha|^2/2) \sum_{n=0}^{\infty} \frac{\alpha^n}{(n!)^{1/2}} \hat{a} |n\rangle \\
&= exp(-|\alpha|^2/2) \sum_{n=1}^{\infty} \frac{\alpha^n}{(n!)^{1/2}} n^{1/2} |n-1\rangle \\
&= \alpha\ exp(-|\alpha|^2/2) \sum_{n=1}^{\infty} \frac{\alpha^{n-1}}{(n-1!)^{1/2}} |n-1\rangle \\
&= \alpha\ exp(-|\alpha|^2/2) \sum_{n=0}^{\infty} \frac{\alpha^n}{(n!)^{1/2}} n^{1/2} |n\rangle \\
&= \alpha |\alpha\rangle
\end{aligned} \tag{2.14}$$

The variance of the photon number is given by:

$$\begin{aligned}(\Delta n)^2 &= \langle\alpha|\,(\hat{n}-\overline{n})^2\,|\alpha\rangle \\ &= \langle\alpha|\,\hat{n}^2\,|\alpha\rangle - 2\overline{n}\,\langle\alpha|\,\hat{n}\,|\alpha\rangle + \overline{n}^2\langle\alpha|\alpha\rangle \\ &= \langle\alpha|\,\hat{n}^2\,|\alpha\rangle - \overline{n}^2 \end{aligned} \tag{2.15}$$

where $\hat{n}$ is the number operator defined as $\hat{n} = \hat{a}^\dagger\hat{a}$. Since consider $\langle\alpha|\,\hat{n}\,|\alpha\rangle = \overline{n}$, using the commutation relation $\left[\hat{a},\hat{a}^\dagger\right] = 1$, Equation 2.15 can be written as

$$\begin{aligned}(\Delta n)^2 &= \langle\alpha|\,\hat{a}^\dagger\hat{a}^\dagger\hat{a}\,|\alpha\rangle - \overline{n}^2 \\ &= \langle\alpha|\,\hat{a}^\dagger(\hat{a}\hat{a}^\dagger - \hat{a}^\dagger\hat{a} + \hat{a}^\dagger\hat{a})\hat{a}\,|\alpha\rangle) - \overline{n}^2 \\ &= \langle\alpha|\,\hat{a}^\dagger(\left[\hat{a},\hat{a}^\dagger\right] + \hat{a}^\dagger\hat{a})\hat{a}\,|\alpha\rangle - \overline{n}^2 \\ &= \langle\alpha|\,\hat{a}^\dagger(1 + \hat{a}^\dagger\hat{a})\hat{a}\,|\alpha\rangle - \overline{n}^2 \\ &= \langle\alpha|\,\hat{a}^\dagger\hat{a}\,|\alpha\rangle + \langle\alpha|\,\hat{a}^\dagger\hat{a}^\dagger\hat{a}\hat{a}\,|\alpha\rangle - \overline{n}^2 \\ &= \langle\alpha|\,\alpha^*\alpha\,|\alpha\rangle + \langle\alpha|\,\alpha^*\alpha^*\alpha\alpha\,|\alpha\rangle\,|\alpha\rangle - \overline{n}^2 \\ &= (\overline{n} + \overline{n}^2) - \overline{n}^2 \\ &= \overline{n} \end{aligned} \tag{2.16}$$

This is the same result found in the Equation 2.7 for the Poissonian photon statistics. We can evaluate $\langle n\,|\alpha\rangle$:

$$\begin{aligned}\langle n\,|\alpha\rangle &= e^{-|\alpha|^2/2}\sum_{m=0}^{\infty}\frac{\alpha^m}{(m!)^{1/2}}\langle n\,|m\rangle \\ &= e^{-|\alpha|^2/2}\sum_{m=0}^{\infty}\frac{\alpha^m}{(m!)^{1/2}}\delta_{nm} \\ &= e^{-|\alpha|^2/2}\frac{\alpha^n}{(n!)^{1/2}} \end{aligned} \tag{2.17}$$

then

$$P(n) = |\langle n\,|\alpha\rangle|^2 = e^{-|\alpha|^2}\frac{|\alpha^2|^n}{(n!)^{1/2}} \tag{2.18}$$

Using the equations 2.14 and the fact that $\hat{n} = \hat{a}^\dagger \hat{a}$, we can obtain the expression for the Poisson distribution as

$$P(n) = \frac{\overline{n}^n}{n!} \exp(-\overline{n}). \tag{2.19}$$

That is exactly Equation 2.5, which gives the expression for the Poisson distribution. By considering of a perfectly coherent field of constant intensity, we can identify different types of light according to the standard deviation of their photon-number distribution. Thus, there are three possibilities:

- $Sub - Poissonian\ statistics: \ \Delta n < \sqrt{\overline{n}}$
- $Poissonian\ statistics: \ \Delta n = \sqrt{\overline{n}}$
- $Super - Poissonian\ statistics: \ \Delta n > \sqrt{\overline{n}}$

In the next subsection we introduce the concept of correlation function that allows us classify the light from another point of view.

2.1.2 Second-order correlation function

Since the invention of the laser, techniques have been created for studying the nonclassical behavior of the light. In particular the resonance fluorescence for a single atom gave us the opportunity of observing photon antibunching and sub-Poissonian photon statistics [22]. Photon antibunching is characteristic of a light field with photons more regularly spaced in time than in a coherent light field.

If we want further information about the statistics of the light field, we need to measure the second-order correlation function which is given by [19, 21]

$$g^{(2)}(\tau) = \frac{\langle E^*(t)E^*(t+\tau)E(t+\tau)E(t)\rangle}{\langle E^*(t)E(t)\rangle\langle E^*(t+\tau)E(t+\tau)\rangle} = \frac{\langle I(t)I(t+\tau)\rangle}{\langle I(t)\rangle\langle I(t+\tau)\rangle} \tag{2.20}$$

where E is the electromagnetic field and I is the intensity of the light beam. In Equation 2.20 we consider measurements of intensity pairs which are detected with a delay time τ.

If we consider a source with a constant intensity such that $\langle I(t)\rangle = \langle I(t+\tau)\rangle$ and assume spatially coherent light the Equation 2.20 can be written as:

$$g^{(2)}(\tau) = \frac{\langle I(t)I(t+\tau)\rangle}{\langle I(t)\rangle^2} \tag{2.21}$$

the correlation function depends only on the relative times of the two intensities being measured, and from this point of view we obtain a symmetry relation that permits realizing calculations only for positive τ values [21]. That expression can be written as:

$$g^{(2)}(-\tau) = g^{(2)}(\tau). \tag{2.22}$$

This is why in this dissertation we will show experimental results only for $\tau > 0$ (see, e.g. Figure 3.6b). One question that appears at this point is how to measure $g^{(2)}(\tau)$, and this is the subject of the next subsection.

2.1.3 Hanbury-Brown and Twiss experiment

The measurement of the correlation of two optical intensities can be expressed in terms of the second-order correlation function using a Hanbury-Brown and Twiss (HBT) apparatus [15,16]. A beam incident on a 50:50 beam splitter is divided in two beams, and each beam strikes on a detector that generates a pulse signal going into an electronic counter that records the time elapsed between the first pulse (called START) in D1 and the second pulse (called STOP) in D2. The corresponding experimental scheme is shown in the Figure 2.2.

Since the number of detected photons (counts) is proportional to the intensity, we can rewrite Equation 2.21 as a function of the counts registered by the detector at time t, as

$$g^{(2)}(\tau) = \frac{\langle n(t)n(t+\tau)\rangle}{\langle n(t)\rangle\langle n(t+\tau)\rangle} \tag{2.23}$$

Here we can express $g^{(2)}(\tau)$ making use of the creation and annihilation operators. Furthermore, we are going to consider that the first photon was detected at time $t = 0$:

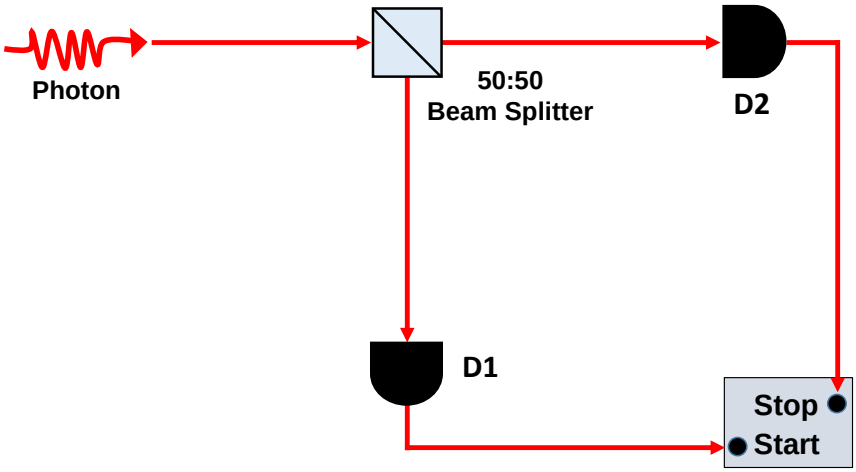

Figure 2.2: Experimental scheme of the Hanbury-Brown and Twiss setup used for realizing the intensity correlation measurements.

$$g^{(2)}(\tau) = \frac{\langle \hat{a}^\dagger(0)\hat{a}^\dagger(\tau)\hat{a}(\tau)\hat{a}(0)\rangle}{\langle \hat{a}^\dagger(0)\hat{a}(0)\rangle\langle \hat{a}^\dagger(\tau)\hat{a}(\tau)\rangle} \tag{2.24}$$

It is helpful to understand the behavior of this correlation function when $\tau = 0$ because it permits to distinguish between different light statistics. So,

$$g^{(2)}(0) = \frac{\langle \hat{a}^\dagger\hat{a}^\dagger\hat{a}\hat{a}\rangle}{\langle \hat{a}^\dagger\hat{a}\rangle\langle \hat{a}^\dagger\hat{a}\rangle} = \frac{\langle \hat{a}^\dagger\hat{a}^\dagger\hat{a}\hat{a}\rangle}{\langle \hat{a}^\dagger\hat{a}\rangle^2} \tag{2.25}$$

Using $\hat{n} = \hat{a}^\dagger\hat{a}$ and the commutation relation $\left[\hat{a}, \hat{a}^\dagger\right] = 1$, the second-order correlation function can be expressed in terms of the photon numbers for $\tau = 0$

$$\begin{aligned} g^{(2)}(0) &= \frac{\langle \hat{a}^\dagger(\hat{a}\hat{a}^\dagger - 1)\hat{a}\rangle}{\langle \hat{a}^\dagger\hat{a}\rangle^2} \\ &= \frac{\langle \hat{n}\hat{n}\rangle - \langle \hat{n}\rangle}{\langle \hat{n}\rangle^2} \\ &= 1 - \frac{1}{n} \end{aligned} \tag{2.26}$$

The last equation gives us an easy way to find out whether the detected light is the result of a coherent source or a single photon emitter. This type of distinction is crucial in the present work because we are looking for single photon emitters. Equation 2.26 depends

only on one variable, n, which is the number of photons emitted. Therefore, measuring $g^{(2)}(0)$ we can know if we are detecting single photons. For example, coherent states reproduce classic electromagnetic wave in the limit of large number of photons. Thus, when $n \to \infty$ we get $g^{(2)}(0) = 1$ for coherent light. If we measure $g^{(2)}(0) = 0$, it means that we have an ideal single emitter. Theoretically, in the especial case that $g^{(2)}(0) = 0$, n can be considered both as number of photons and/or number of emitters. However, to obtain $g^{(2)}(0) = 0$ experimentally is not possible due to the electronic noise generated in the APDs and the efficiency limited by their dead time. In this sense it is enough for us to obtain $0 < g^{(2)}(0) < 0.5$ ($g^{(2)}(0) = 0.5$ when $n = 2$) because with that we strictly verify the detection of single emitter [19, 21–23].

2.1.4 Bunching and antibunching

Another way to classify the types of light is looking at the value of $g^{(2)}(0)$, as shown below:

- *Bunched light* : $g^{(2)}(0) > 1$
- *Coherent light* : $g^{(2)}(0) = 1$
- *Antibunched light* : $g^{(2)}(0) < 1$

Obtaining $g^{(2)}(0) = 1$ implies that the probability of getting a stop pulse in D2 for each measurement of correlation will always be the same for all values of τ. $g^{(2)}(0) > 1$ is characteristic for thermal light. It consists of bunches of photons, meaning that if we detect one photon in $t = 0$ there is a high probability of detecting another photon in a short time after. When we measure $g^{(2)}(0) < 1$ we categorize them as non-classical light, for this type of light, photons come out from the source with more regular time gaps between them than from coherent sources. This means that two events seldom occur simultaneously and the probability of detecting a photon after detecting another one is very small for small values of τ.

So far, we have covered some properties concerning light, regarding fundamentally coherent light and detection of single photons that is the basis for the development of our

experiments. We also learned some important characteristics of the different types of light. With the interpretation of the second-order correlation function we can know whether we are detecting light from a single-photon emitter, what is fundamental in the development of this work.

The sources in which we are interested in studying here must be single photon emitters. We consider now quantum systems with optical transitions, whose fundamental level is defined by their spin states, that can be modelled as a two level system, for which we will study their dynamics.

2.2 Coherent dynamics in a two level system

In this section, the time evolution of a two level system will be studied in the formalism of the density matrix operator. Here the effect of the environment will be considered phenomenologically, by introducing a relaxation parameter. We also give a geometrical interpretation of the density operator through the Bloch vector and introduce the concept of π pulses that are able to invert the system populations. In a two level system the evolution of the density operator is described by the optical Bloch equations. Their steady state solution allows the interpretation of the power broadening phenomenon. Finally, we will study the coherent oscillations of the populations between two levels known as Rabi oscillations [24]. In our system there are two spin levels of the electronic ground state of NV^- defects in nanodiamonds.

2.2.1 Density operator

To study the light-matter coupling and provide a description at time of a quantum system state, we introduce here the density operator ($\hat{\rho}$) formalism. $\hat{\rho}(t)$ is defined as [22, 25]

$$\hat{\rho}(t) = |\varphi(t)\rangle \langle\varphi(t)| \tag{2.27}$$

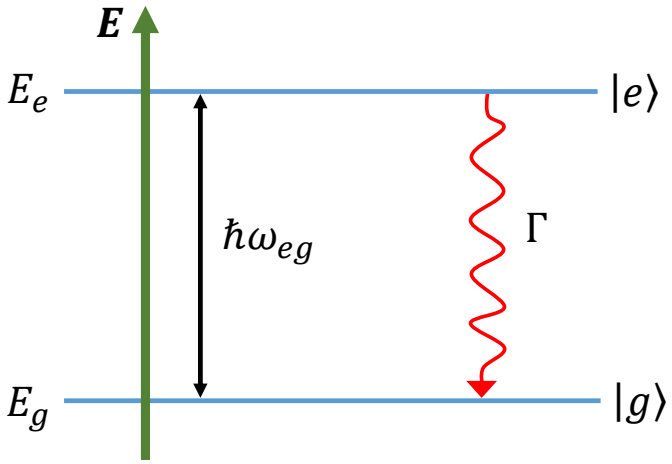

Figure 2.3: Schematics of a two level system.

and the matrix elements of $\hat{\rho}(t)$ are:

$$\rho_{mn}(t) = \langle\varphi_m|\,\hat{\rho}(t)\,|\varphi_n\rangle = c_m^*(t)c_n(t) \tag{2.28}$$

where $c_m^*(t)$, $c_n(t)$ are complex numbers that fulfill the condition $|c_m|^2 + |c_n|^2 = 1$. In our experiments, we work with nanoparticles which have a spin state that can be modelled as a two level system, so we can define the state of a system $|\varphi\rangle$ as a linear combination of states $|g\rangle$ and $|e\rangle$. Thus, $|\varphi\rangle = c_g\,|g\rangle + c_e\,|e\rangle$, with $|g\rangle$ and $|e\rangle$ as the ground and excited states respectively, as shown in Figure 2.3.

The matrix elements ρ_{mn} of the density matrix $\hat{\rho} = |\varphi\rangle\langle\varphi|$ (time dependence implicit) are:

$$\begin{aligned}
\rho_{gg} &= \langle g|\,\hat{\rho}(t)\,|g\rangle = c_g c_g^* \\
\rho_{ee} &= \langle e|\,\hat{\rho}(t)\,|e\rangle = c_e c_e^* \\
\rho_{ge} &= \langle g|\,\hat{\rho}(t)\,|e\rangle = c_g c_e^* = \rho_{eg}^*
\end{aligned} \tag{2.29}$$

The matrix representation of the density operator is

$$\hat{\rho} = \begin{pmatrix} \rho_{gg} & \rho_{ge} \\ \rho_{eg} & \rho_{ee} \end{pmatrix}. \tag{2.30}$$

The diagonal elements ρ_{mm} are known as terms of population while the off-diagonal elements ρ_{mn} are called terms of coherence. The temporal evolution of $\hat{\rho}$ is described by [25]

$$i\hbar\frac{d\hat{\rho}}{dt} = [\hat{H}, \hat{\rho}]. \tag{2.31}$$

This equation involves the commutator between the system Hamiltonian and the density operator and is known as the von Neumann equation.

In order to understand the dynamics of a two level system in a simple way, a geometrical point of view is used. In the next section we will introduce and study the Bloch vector U(t) and its time evolution when a radiation pulse is applied to the system.

2.2.2 Bloch vector and π pulses

Now we introduce a geometrical representation which allows us to understand in a simple way the time evolution of a two-level system. In this picture, the geometrical interpretation of coherent superposition states is called the Bloch representation. The vector that describes the state is called Bloch vector, and the sphere that it defines is called Bloch sphere [19].

We define U(t) in a rotating system with the frequency ω of an applied field $E(t)$ nearly in resonance with the transition of interest. In this rotating reference frame, the components of the Bloch vector are u, v, w such that [26]

$$u^2 + v^2 + w^2 = 1 \tag{2.32}$$

where

$$u(t) = u_0 \tag{2.33}$$

$$v(t) = w_0 \sin\theta(t) + v_0 \cos\theta(t) \tag{2.34}$$

$$w(t) = -v_0 \sin\theta(t) + w_0 \cos\theta(t) \tag{2.35}$$

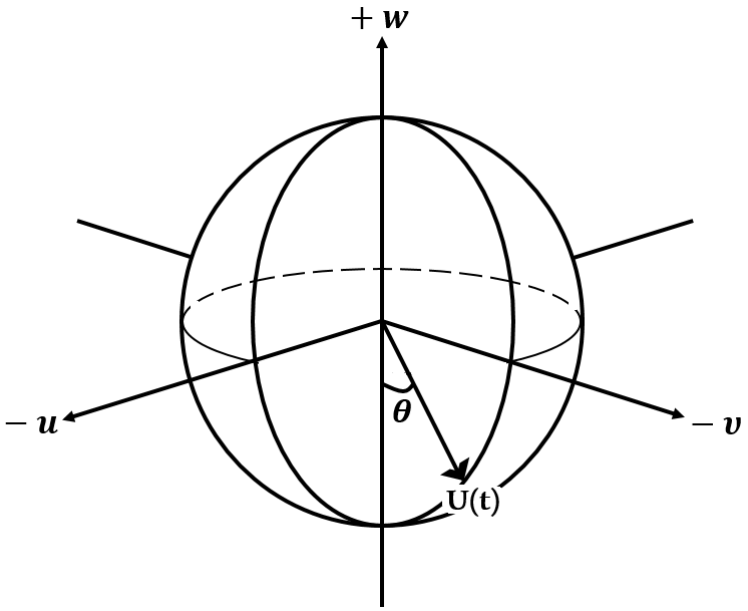

Figure 2.4: Bloch vector U(t) and the Bloch sphere. The θ angle is defined in the Equation 2.39 and has direct meaning only for atoms exactly in resonance with the field. $\theta(t)$ is in the $v - w$ plane.

$w(t)$ is a population difference in a two level system, which is called the inversion. $v(t)$ is the absorptive component of the dipole moment, while $u(t)$ is the dispersive component. u_0, v_0 and w_0 are the components of U(0) and are defined as

$$u_0 = \rho_{eg} + \rho_{ge} \tag{2.36}$$

$$v_0 = -i(\rho_{eg} - \rho_{ge}) \tag{2.37}$$

$$w_0 = \rho_{gg} - \rho_{ee} \tag{2.38}$$

Here we will assume that the vector realizes a rotation about the u axis (Figure 2.4). $\theta(t)$ is defined by the relation [26]

$$\theta(t) = \int_{t_1}^{t_2} \frac{dE(t)}{\hbar} dt \tag{2.39}$$

where d is magnitude of the dipole matrix element and $E(t)$ is the projection of the applied field along of the dipole moment (or $E(t)$ is the applied field and d is the projection of the dipole moment along it). In the case in which the applied field has the steady value E_0 between t_1 and t_2, the solution of the integral given in Equation 2.39 is:

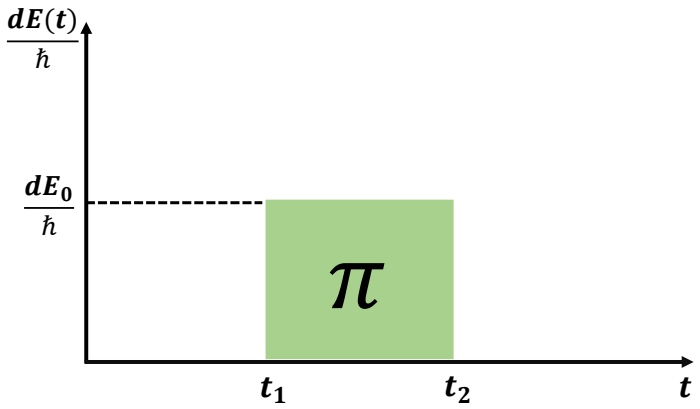

Figure 2.5: Square pulse of a coherent field which area is π .

$$\theta(t) = \frac{dE_0}{\hbar}(t_2 - t_1) = \Omega(0)(t_2 - t_1) \tag{2.40}$$

where $\Omega(0) = dE_0/\hbar$ is called the Rabi frequency on resonance. It indicates the rate at which transitions are coherently induced by the electromagnetic filed in a two level system. Considering the system initially in the ground state ($w_0 = -1$ and $\upsilon_0 = 0$), after a time $\Delta t = t_2 - t_1$ such that $\Omega\Delta t = \pi$, Equation 2.35 shows $w = +1$. That means the population of the system is promoted to the excited state. Another way to see this fact is considering a coherent field in a square wave form such that the area $A(t)$ enclosed by this pulse is equal to π (Figure 2.5). This is called a π pulse. Then we can write

$$A(t) = \theta(t) = \int_{t_1}^{t_2} \frac{dE(t)}{\hbar} dt \tag{2.41}$$

Thus, resonant pulses with an area that is multiple of π, for instance, π, 2π, 3π, can invert the populations 1, 2, 3, times. Another type of pulses that exist and that indirectly are used in our experiments, (however it will be crucial in future experiments, which are commented in the perspectives) are called $\pi/2$ pulses. These pulses create a coherent superposition between the spin states on the $\upsilon - w$ plane. The development of this section is very useful to understand the evolution of the transitions in a two level system that are explained in the next sections.

2.2.3 Optical Bloch equations

The optical Bloch equations describe the time evolution of the atomic populations and the coherences within the formalism of the density operator [21,25]. That means they are the equations of motion for the density matrix elements. This is useful to understand the behavior of transient phenomena in a two level system (Figure 2.3).

The total Hamiltonian $\hat{H}_T$ that describes the system is composed by the unperturbed Hamiltonian $\hat{H}_0$, the interaction Hamiltonian $\hat{H}_I$ and the relaxation Hamiltonian $\hat{H}_R$, so the $\hat{H}_T$ can be written as

$$\hat{H}_T = \hat{H}_0 + \hat{H}_I + \hat{H}_R \tag{2.42}$$

The unperturbed Hamiltonian is defined in absence of external fields and relaxation processes, and can be written as

$$\hat{H}_0 = \begin{pmatrix} E_g & 0 \\ 0 & E_e \end{pmatrix} \tag{2.43}$$

Now, considering the presence of an electric field $\hat{E}(t) = \hat{E}_0 cos\omega t$, the interaction Hamiltonian is $\hat{H}_I = -\hat{\mu} \cdot \hat{E}(t)$, in the dipole approximation:

$$\hat{H}_I = -\hat{\mu} \cdot \hat{E}_0 cos\omega t \tag{2.44}$$

Due to the parity the dipole operator $\langle g| \hat{\mu} |g\rangle = \langle e| \hat{\mu} |e\rangle = 0$, only the dipole matrix elements $d = \langle g| \hat{\mu} |e\rangle = \langle e| \hat{\mu} |g\rangle$ are nonvanishing. Thus, the interaction Hamiltonian operator can be written as

$$\begin{aligned} \hat{H}_I &= \begin{pmatrix} 0 & -h\Omega cos\omega t \\ -h\Omega cos\omega t & 0 \end{pmatrix} \\ &= \begin{pmatrix} 0 & -\frac{h\Omega}{2}(e^{i\omega t} + e^{-i\omega t}) \\ -\frac{h\Omega}{2}(e^{i\omega t} + e^{-i\omega t}) & 0 \end{pmatrix} \end{aligned} \tag{2.45}$$

where

$$\Omega = \frac{dE_0}{\hbar} \tag{2.46}$$

is again the Rabi frequency on resonance.

The last term of the Hamiltonian $\hat{H}_R$ is responsible for relaxation processes. We write it introducing phenomenological decay constants Γ and γ, respectively the decay rates of the population and coherence terms. In this way, we can write (see Equation 2.31) [25]

$$[\hat{H}_R, \hat{\rho}] = i\hbar \begin{pmatrix} \Gamma\rho_{ee} & -\gamma\rho_{ge} \\ -\gamma\rho_{eg} & -\Gamma\rho_{ee} \end{pmatrix} \tag{2.47}$$

$\Gamma = 1/T_e$ is the excited state decay rate where T_e is its lifetime and $\gamma = 1/T_c$ is the coherence decay rate due to for instance interaction with the local environment. Generally, in the literature T_e is called longitudinal relaxation time and is labeled as T_1, while T_c is known as transverse relaxation time or T_2 time. Additionally, also exists a term related to dephasing effects and is labeled as T_2^*, which is the time scale on which states of the two level system accumulate a random phase relative to one another. Is known that $T_1 \gg T_2 \gg T_2^*$ [26].

Inserting these terms in Equation 2.31, which gives us the temporal evolution of the system, we can find an equation system that allows us to know the behavior of the complete dynamics of a two level system when interacting with a radiation field. This equation system is known as the optical Bloch equations, and can be written as

$$\begin{aligned}
i\hbar\tfrac{d}{dt}\rho_{gg} &= \tfrac{i\Omega}{2}(\rho_{eg} - \rho_{ge})(e^{i\omega t} + e^{-i\omega t}) + i\hbar\Gamma\rho_{ee} \\
i\hbar\tfrac{d}{dt}\rho_{ge} &= \tfrac{i\Omega}{2}(\rho_{ee} - \rho_{gg})(e^{i\omega t} + e^{-i\omega t}) + \rho_{ge}(E_1 - E_2) - i\hbar\gamma\rho_{ge} \\
i\hbar\tfrac{d}{dt}\rho_{eg} &= \tfrac{i\Omega}{2}(\rho_{gg} - \rho_{ee})(e^{i\omega t} + e^{-i\omega t}) + \rho_{ge}(E_2 - E_1) - i\hbar\gamma\rho_{eg} \\
i\hbar\tfrac{d}{dt}\rho_{ee} &= \tfrac{i\Omega}{2}(\rho_{ge} - \rho_{eg})(e^{i\omega t} + e^{-i\omega t}) - i\hbar\Gamma\rho_{ee}
\end{aligned} \tag{2.48}$$

We can define a frequency in function of the energy difference $\omega_{ij} = (E_i - E_j)/\hbar$ and the detuning $\Delta = \omega_{eg} - \omega$. Furthermore, in order to solve this system of equations we can use the Rotating Wave Approximation (RWA), that consists in transforming the Hamiltonian

into the rotating frame, which rotates at the frequency of the ω. To do that, we introduce the following substitutions:

$$\begin{aligned} \rho_{ge} &= \rho'_{ge} e^{i\omega t} \\ \rho_{eg} &= \rho'_{eg} e^{-i\omega t} \end{aligned} \tag{2.49}$$

The RWA allows to neglect effects that are associated with oscillations at twice the optical frequency [26]. With this simplification, the equation system in 2.48 turns to

$$\begin{aligned} \tfrac{d}{dt}\rho_{gg} &= \tfrac{i\Omega}{2}(\rho'_{eg} - \rho'_{ge}) + \Gamma\rho_{ee} \\ \tfrac{d}{dt}\rho'_{ge} &= \tfrac{i\Omega}{2}(\rho_{ee} - \rho_{gg}) + (\gamma + i\Delta)\rho'_{ge} \\ \tfrac{d}{dt}\rho'_{eg} &= \tfrac{i\Omega}{2}(\rho_{gg} - \rho_{ee}) + (\gamma - i\Delta)\rho'_{eg} \\ \tfrac{d}{dt}\rho_{ee} &= \tfrac{i\Omega}{2}(\rho'_{ge} - \rho'_{eg}) - \Gamma\rho_{ee} \end{aligned} \tag{2.50}$$

These equations are used to describe the dynamics of a spin state due to the influence of a magnetic field in analogy with the influence of an optical field on a two level system. We can give a solution to this equation system 2.50 in the steady state if we set them equal to zero. The result for ρ_{ee} is

$$\rho_{ee} = \frac{\gamma\Omega^2}{2(\Gamma\Delta^2 + \gamma^2\Gamma + \gamma\Omega^2)}. \tag{2.51}$$

We can consider that there is no environment contact but only spontaneous decay, so we can write $2\gamma = \Gamma$ [21] to obtain a reduced expression of the Equation 2.51

$$\rho_{ee} = \frac{\Omega^2}{4\Delta^2 + \Gamma^2 + 2\Omega^2} \tag{2.52}$$

In the last equation, the presence of Ω^2 in the denominator causes a broadening in the linewidth of the transition $|g\rangle \rightarrow |e\rangle$. This phenomenon is known as power broadening. Figure 2.6 shows this effect and we can observe that the population asymptotically approaches the value 0.5 that is when the system is saturated. So, when we talk about power broadening we do not take into account only the linewidth due to the spontaneous emission (also known as natural linewidth), but also that now we have saturation effects that give us a more general expression for the linewidth as [21]

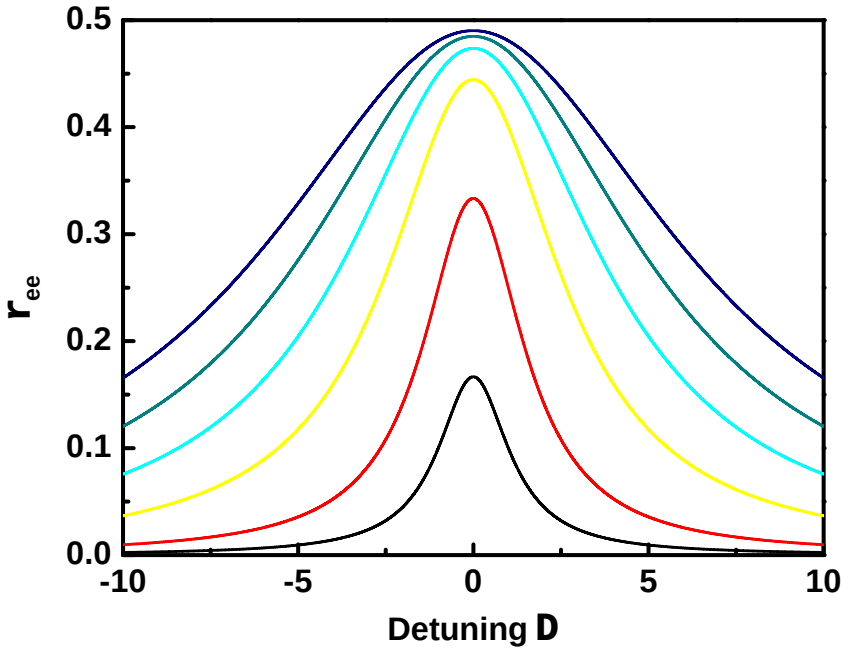

Figure 2.6: Illustration of the power broadening effect. The curves from bottom to top are obtained with $\Gamma = 1$ MHz and $\Omega = 1$, 2, 4, 6, 8 and 10 MHz respectively.

$$2\left(\gamma^2 + \frac{1}{2}\Omega^2\right)^{1/2}. \tag{2.53}$$

This equation will be useful when analyzing the results in subsection 3.4.2 where the power broadening of the ODMR spectrum is shown.

2.2.4 Rabi oscillations

We can find solutions for the optical Bloch equations in some special cases using a trial function not taking into account the effects of the damping (that means $\Gamma = \gamma = 0$) as [21]

$$\rho_{ij} = \rho_{ij}^{(0)} e^{\lambda t} \tag{2.54}$$

Furthermore, writing the initial conditions as

$$\begin{aligned} \rho_{22}(0) &= 0 \\ \rho_{12}(0) &= 0 \end{aligned} \tag{2.55}$$

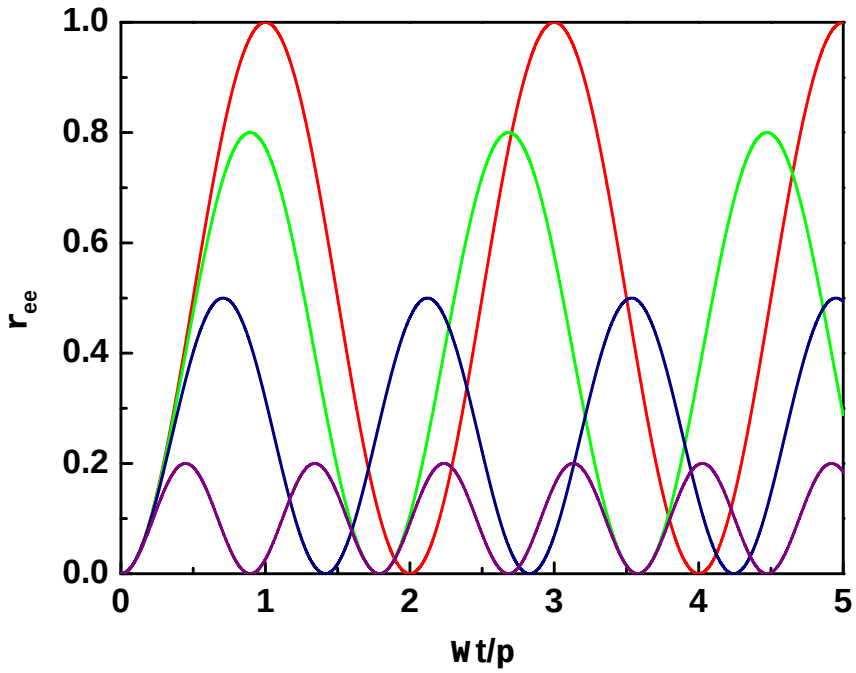

Figure 2.7: Rabi oscillations for different detunings with a fixed frequency $\Omega = 1$ in absence of damping. We can observe that the oscillations maintain a constant amplitude all the time for each value of Δ. $\Delta = 0$ (Red), $\Delta = \Omega/2$ (Green), $\Delta = \Omega$ (Blue) and $\Delta = 2\Omega$ (Violet).

we can obtain a simplified equation for the dynamics of the excited state

$$\rho_{ee}(t) = \frac{\Omega^2}{\Omega'^2} sin^2\left(\frac{\Omega'}{2}t\right) \tag{2.56}$$

In the above equation, $\Omega' = \sqrt{\Omega^2 + \Delta^2}$ is the generalized Rabi frequency. Examples of this dynamics are shown in the Figure 2.7 for different values of Δ. The degree of excitation oscillates between 0 and Ω^2/Ω'^2 obtaining the maximum population inversion when a pulse with area of π, 2π, 3π, and so on is applied [26]. The oscillatory behavior between the ground and excited states have a frequency Ω'. For values $\Delta > 0$ we obtain higher frequency values with smaller amplitudes then in the resonant case.

In a real physical situation the system presents damping, i.e., losses due to energy radiated by oscillation of dipoles in interaction with the radiation field or any kind of dephasing process that makes the dipoles to be completly out of phase in relation to each other such that the polarization density may be zero. When we include the damping effects (this

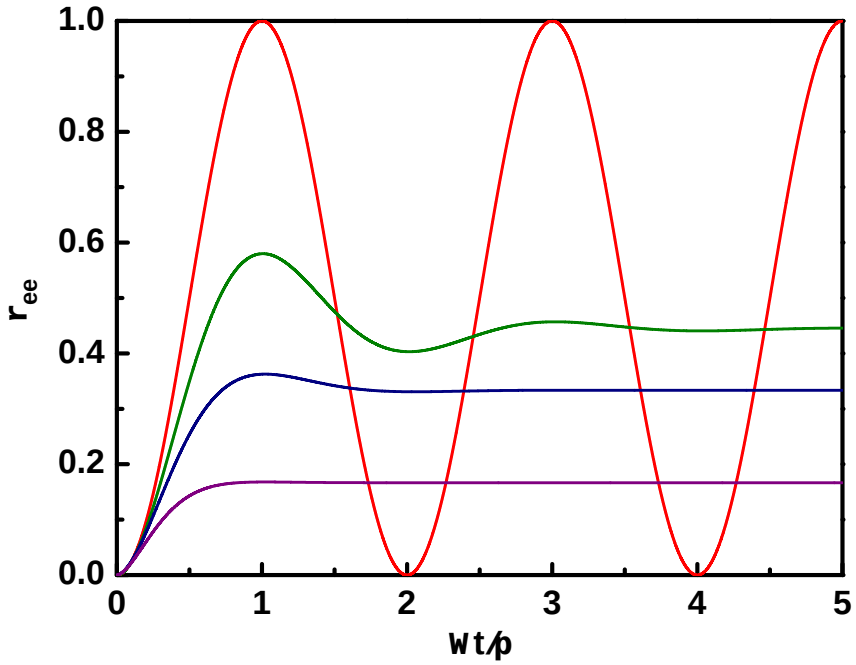

Figure 2.8: Rabi oscillations in presence of damping ($\Delta = 0$). The figure shows oscillations for different values of γ observing damping when $\gamma \to \Omega$: $\gamma = 0$ (Red), $\gamma = \Omega/4$ (Green), $\gamma = \Omega/2$ (Blue), $\gamma = \Omega$ (Violet).

means Γ, $\gamma \neq 0$), it is impossible to analytically resolve the equations system 2.50 in a general way, so we assume solution in the resonant case, $\Delta = 0$, with the same initial conditions given in 2.55 to obtain [21]

$$\rho_{ee}(t) = \frac{\Omega^2/2}{2\gamma^2 + \Omega^2}\left[1 - \left(cos\lambda t + \frac{3\gamma}{2\lambda} sin\lambda t\right)e^{-\frac{3\gamma t}{2}}\right] \tag{2.57}$$

where

$$\lambda = \left(\Omega^2 - \frac{1}{4}\gamma^2\right)^{1/2} \tag{2.58}$$

The exponential term is the responsible for modulating the oscillation amplitude. The curve for $\gamma = 0$ reproduces the same oscillations given by Equation 2.56. Examples of such dynamics are shown in the Figure 2.8 with increasing γ. We can observe that the oscillations are rapidly damped until we stop to see them when $\gamma \to \Omega$. The effect of the relaxation is thus a modulation of the oscillations amplitude in the population dynamics.

2.3 Single nitrogen-vacancy defect in diamond

The nitrogen-vacancy center is a promising candidate to be used in different applications because it exhibits long coherent times and high photostability at room temperature [27]. In the following, we discuss their basic optical and spin properties and the photophysics involved in transitions among the defects' energy levels.

2.3.1 Structure and properties of single NV defects in nanodiamonds

There exist more than one hundred luminescent defects in diamond that are widely studied [4]. Due to their stability and their interesting optical properties, they are often artificially embedded in nanocrystals that can be used as single photon sources or as fluorescent biomarkers because they are protected by the diamond structure, presenting high stability and low cytotoxicity [28]. In this work, we are interested in the nitrogen-vacancy (NV) defect [29].

The NV defect in diamond presents a trigonal symetry C_{3v} [4, 30], that consists of a substitutional nitrogen atom and a vacancy in an adjacent site of the diamond lattice, as shown in the Figure 2.9. That means that two lattice sites that should be occupied by carbon atoms were altered. One carbon atom is replaced by a nitrogen atom and other site lattice is replaced by an empty space (the vacancy). This structure can be formed with a process of irradiation with thermal neutrons followed by annealing in a nitrogen rich atmosphere [31, 32].

The nitrogen atom belongs to the V group of the periodic table, therefore it has five valence electrons: three are shared with the three nearest carbon atoms and two are located in the dangling bonds in the direction of the vacant site. The NV defects can appear in two types, the first is known as a neutral NV^0 defect that has five electrons: three of the carbon and two of the nitrogen. Thus, around the vacant site, there are five electronic bonds which are: two due to the nitrogen atom and three due to carbon atoms. In this structure, one of the electrons is unpaired and the interaction among these five

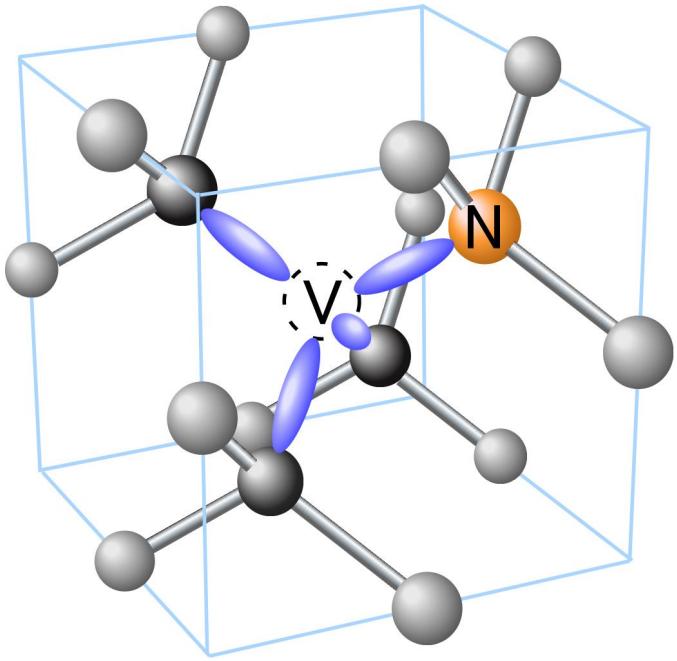

Figure 2.9: Diamond crystallographic structure with the scheme of a NV defect consisting of a substitutional nitrogen atom next to a missing carbon atom (a vacancy) [27].

electrons results in a total spin $S = 1/2$. Therefore the ground state of this configuration is a singlet. Other configuration of the NV is presented when an additional electron from the lattice, probably from another substitutional nitrogen atom, is captured by the defect [32]. There will then be six electrons occupying the dangling bonds of the vacancy complex [33]. This configuration is known as negatively charged NV^- defect. Each one of the three carbon atoms has four symmetrical bonds, one pointing at the vacant site and the others pointing at the other carbon atoms in the lattice. Similarly, the nitrogen atom has one bond pointing at the vacant site and the other pointing at the carbon atoms.

For the negatively charged NV^- defect, electron spin resonance indicates that the defect has a paramagnetic electronic state with total spin angular moment $S = 1$ which has a spin triplet (^3A) ground state and excited (^3E) triplet state (Figure 2.10a). Spin-spin interaction splits the (^3A) ground state by $D = 2.87$ GHz into a state spin projection $m_s = 0$ and a degenerated doublet with $m_s = \pm 1$ [11], which is known as zero field splitting. Correspondingly, the exited state is split by $D' = 1.43$ GHz. The crystal field splitting quantizes the spin states along the N-V symmetry axis, so that in the presence

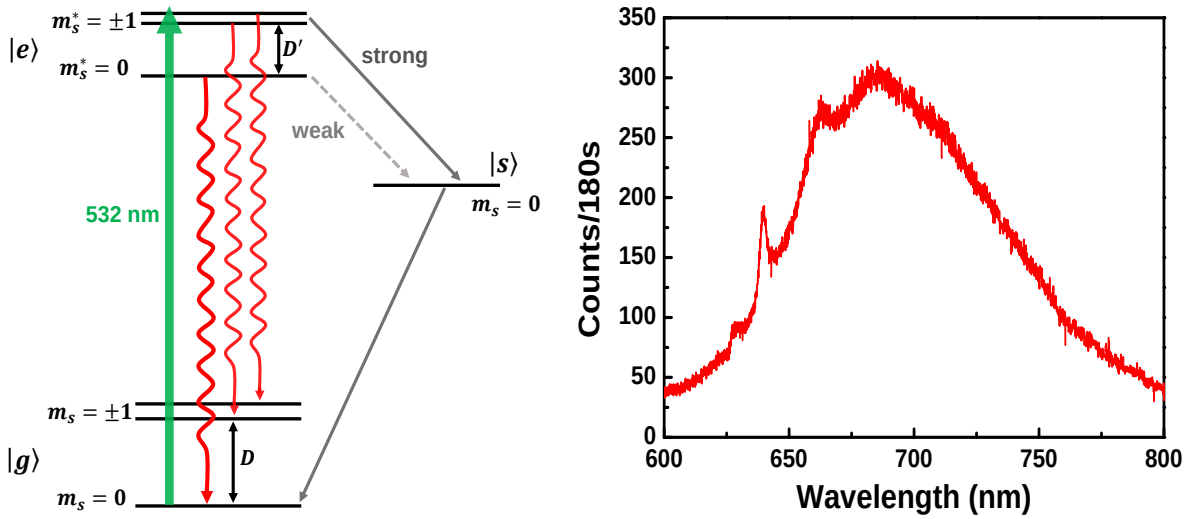

Figure 2.10: (a) NV^- electronic levels, showing the dynamics of the system in the process of optical excitation (thick upward arrow) and emission of fluorescence (curly arrows). Also represented are non-radiative decay processes (thin arrows) (b) Fluorescence spectrum of a single NV^- center with a characteristic zero phonon line (ZPL) at 637 nm, taken at room temperature under the excitation of a CW laser emitting at 532 nm.

of an external magnetic field, the $m_s = \pm 1$ sublevels will have an energy splitting that is proportional to the projection of the field along of the N-V axis, that is, the degeneracy of the states with spin projection $m_s = \pm 1$ can be lifted by means of the Zeeman effect [34].

The spin Hamiltonian of the nitrogen-vacancy defect can be written as the sum of zero field spliting and Zeeman terms as [35]

$$H_S = D\{S_z^2 - (1/3)[S(S+1)]\} + g\mu_B \bar{B} \cdot \bar{S} \tag{2.59}$$

where μ_B is the Bohr magneton and g is the electron g-factor ($g \approx 2.0$). $\bar{B}$ is the external magnetic field.

Pure diamond has an energy gap of 5.5 eV. The NV^- center, which is an intragap defect, shows strong optical transitions between the ground and the excited states, which present a separation in energy of 1.95 eV., allowing the detection of individual NV^- defects at room temperature using optical confocal microscopy. The electronic structure (see Figure 2.10a) and its photophysics (see next section) allow it to be optically polarized (initialized)

and coherently manipulated and read out by a technique known as Optically Detected Magnetic Resonance (ODMR) [36].

2.3.2 Photophysics of the NV^- defect in nanodiamonds

To explain the photophysics of a single NV^- defect, we will define the triplet ground state with $m_s = 0$ and $m_s = \pm 1$ sublevels, and a triplet excited state with $m_s^* = 0$ and $m_s = \pm 1$ as well as a metastable singlet state with $m_s = 0$, as shown in Figure 2.10a. In our experiment we drive a transition towards the excited state by means of a linearly polarized CW laser emitting at 532 nm. These transitions are subjected to spin angular momentum conserving selection rules and to lead transitions between the triplet states with a characteristic fluorescence with a zero-phonon line (ZPL) at 637 nm and a broad phonon-sideband extended up to 800 nm at room temperature (Figure 2.10b). The transition $m_s = 0 \rightarrow m_s^* = 0$ results in a predominantly radiative decay while for transitions that occurs between the $m_s = \pm 1$ sublevel to the exited $m_s^* = \pm 1$ sublevels, the system has a higher probability to decay via intersystem crossing to the metastable singlet state and then to the $m_s = 0$ of the triplet ground state with a non-radiative decay path. This process permits to drive the NV^- defect into $m_s = 0$ ground state [32]. When this occurs it is said that the system was spin polarized by optical pumping. This characteristic is important for quantum information protocols [37]. Due to the fact that the decay from the $m_s^* = \pm 1$ state, by mean of the intersystem crossing, towards the metastable state is more probable, the fluorescence intensity drops in approximately a 30%. Following this path the system doesn't emit fluorescence compared with the decay from $m_s^* = 0$. The radiative lifetime of the excited state is approximately 20 ns [28].

Using a microwave field the paramagnetic ground state can be coherently manipulated between the $m_s = 0$ and $m_s = \pm 1$ Zeeman sublevels. This permits to have control of the transitions, obtaining population inversion between those two levels. To know the spin state, we should detect the fluorescence and observe its intensity that gives us information about it. In this sense we are interested in knowing what is the microwave frequency that

induces a transition between the sublevels of the ground state lowering the fluorescence that we detect. This is the essence of the ODMR technique.

So far, we studied the theoretical part that will be useful to understand the physics which explains the different phenomena that were observed during the experiment. In the next section we introduce the Scanning Confocal Optical Microscopy technique which is an important tool that allows us to obtain images with high resolution. Despite being a technique developed to study biological systems, it becomes very important for us by the reasons explained below.

2.4 Scanning Optical Confocal Microscopy

Optical microscopy is widely used in many branches of science, particularly in studying biological systems [38]. Most samples investigated with optical microscopy have reflective surfaces that present imperfections such that the light interacts with them in different depths and the images seen by the observer present blurring, producing a degradation in the contrast and the resolution. To overcome these problems, confocal microscopy was developed by Marvin Minsky and applied to image neural networks of brain tissue [39]. The principle of this technique is based on eliminating the light reflected or fluorescence originated in perifocal regions using a pinhole in the detection path. As shown in Figure 2.11a, the emitted signal by the particle/fluofore located in the illuminated spot comes back via the same optical path, passes through a dichroic mirror and focusses onto a detector after passing through a pinhole, which is the essential difference of the confocal technique in relation to the usual microscopy. As a result, with a confocal microscope we can obtain better sharpness and contrast in the image and higher transversal and axial resolutions.

The resolution of an optical system is given by its Point Spread Function (PSF), which is basically the diffraction pattern that arises when a point object is imaged through the optical system (lenses, apertures, etc.) [40]. The PSF ($\mathscr{P}$) of a circular aperture in the paraxial approximation has the form of an Airy disc [18]

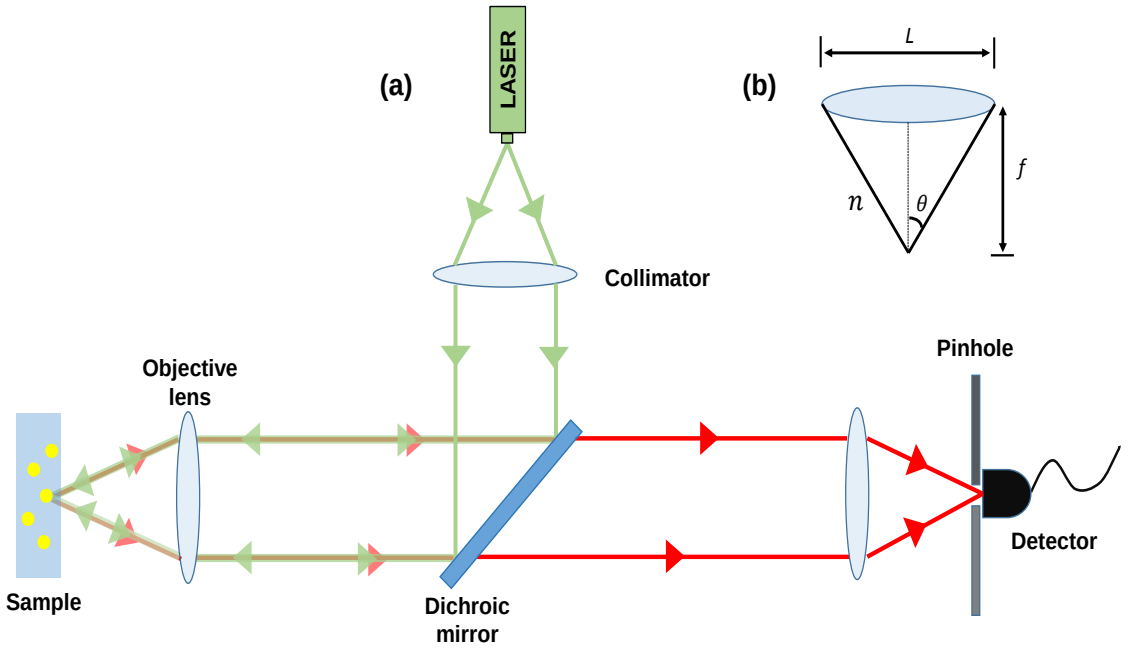

Figure 2.11: (a) Simplified scheme of a confocal microscope. Light coming out of the laser source hits over the surface of the dichroic mirror and is reflected towards the sample. The fluorescence emitted is allowed to pass through the dichroic mirror to the detector. (b) Schematics of an objective lens. L is the diameter, n the refractive index and f the focal distance.

$$\mathscr{P} = \left[\frac{2J_1(\alpha r)}{\alpha r}\right]^2 \tag{2.60}$$

where $\alpha = 2\pi \text{N.A.}/\lambda$ and $J_1(\alpha r)$ is the Bessel function of the first kind. λ is the wavelength of the light and $\text{N.A.} = n \sin\theta$ is the numerical aperture of the objective, where n is the refractive index of the medium and θ is the half angle of the maximum cone of light converging or diverging from an illuminated spot, as Figure 2.11b shows. The first zero of the function $J_1(\alpha r)$ is located at $\alpha r = 3.823$ or $r = 0.61\lambda/\text{N.A.}$ The width between the half-power points of the main lobe of $\mathscr{P}$ is known as the full width half-maximum (FWHM) and is given by [40]

$$\text{FWHM} = \frac{0.51\lambda}{nsin\theta} = \frac{0.51\lambda}{\text{N.A.}}. \tag{2.61}$$

This formula for the width of the image of a point object is also called "the single point resolution" of the standard optical microscope and it means that the image of a point object will be better resolved if the FWHM is as narrow as possible. According to this equation the resolution of an optical microscope is determined by the numerical aperture. So, the resolution can be improved by using immersion objectives with high refractive index which increases the N.A. and consequently reduces the FWHM.

In the confocal microscope, the pinhole significantly reduces the background that is typical of a conventional fluorescence microscope, because the focal point of the objective lens forms an image where the pinhole is, those two points are known as "conjugate points" (or alternatively, the plane of the sample and the pinhole are conjugate planes). The pinhole is conjugate to the focal point of objective lens, hence the name "confocal". This is clearly seen in the simplified scheme of the confocal microscope shown in the Figure 2.11a.

In the standard microscope the PSF is mainly determined by the microscope objective but in the case of confocal microscopy we have to add a new PSF that appear due to a new aperture (PINHOLE) resulting in an effective PSF given by the square of the PSF for a standard microscope or $\mathscr{P}^2$ [40]

$$\mathscr{P}_c = \mathscr{P}^2 = \left\{ 2\Big[\frac{J_1(\alpha r)}{\alpha r}\Big]^2 \right\}^2 \tag{2.62}$$

Figure 2.12 shows the intensity profile for both conventional microscope and confocal microscope. Notice that the curve corresponding to the confocal microscope is narrower, fact that evidences its higher resolution.

The single point resolution for the confocal microscope is defined as the half-power width of the main lobe of the $\mathscr{P}^2$,

$$\mathrm{FWHM_C} = \frac{0.37\lambda}{nsin\theta} = \frac{0.37\lambda}{\mathrm{N.A.}} \tag{2.63}$$

So, the definition of single-point to a confocal microscope is 28% better than the resolution of the standard optical microscope. In practice, when investigating single scatterers or

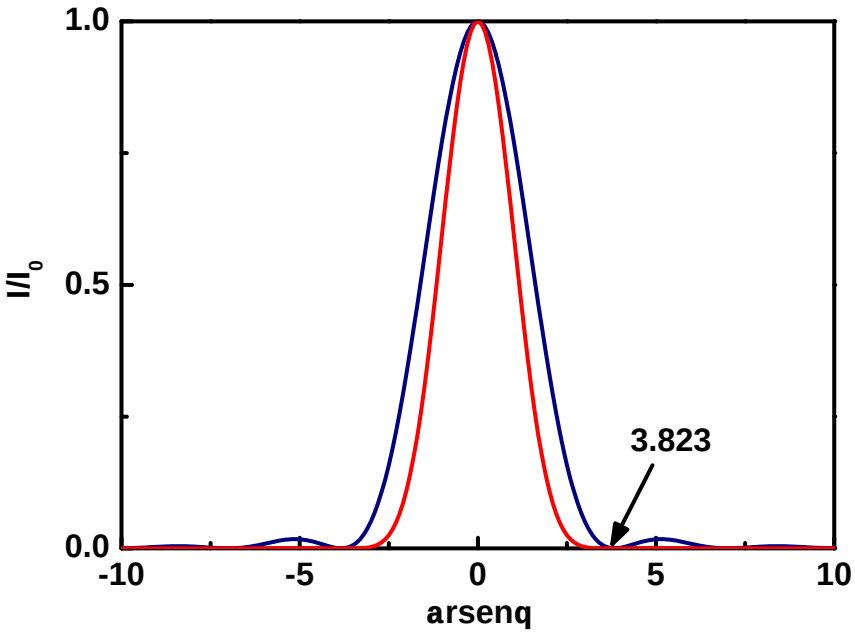

Figure 2.12: Intensity profile of the PSF to a conventional microscope (blue curve) and a confocal microscope (red curve).

emitters much smaller that the wavelength, the FWHM of the intensity profile of the illuminated point object is used as criterion for the estimation of the resolution of our optical system.

To define the minimal distance in which two illuminated points can be resolved we make use of the Rayleigh criterion, which states that two closely spaced illuminated points are distinguishable from each other when the first minimum of the diffraction pattern of one source point coincides with the maximum of the pattern of other. For light with wavelength λ, this minimum distance d is given by the Rayleigh criterion for the confocal microscopy [40] (see Figure 2.13).

$$\mathrm{d} = \frac{0.56\lambda}{\mathrm{N.A}} \tag{2.64}$$

With this result, we conclude the theoretical part of this dissertation and now we will pass to the next section where we will use this theory to explain the results obtained in our experiments.

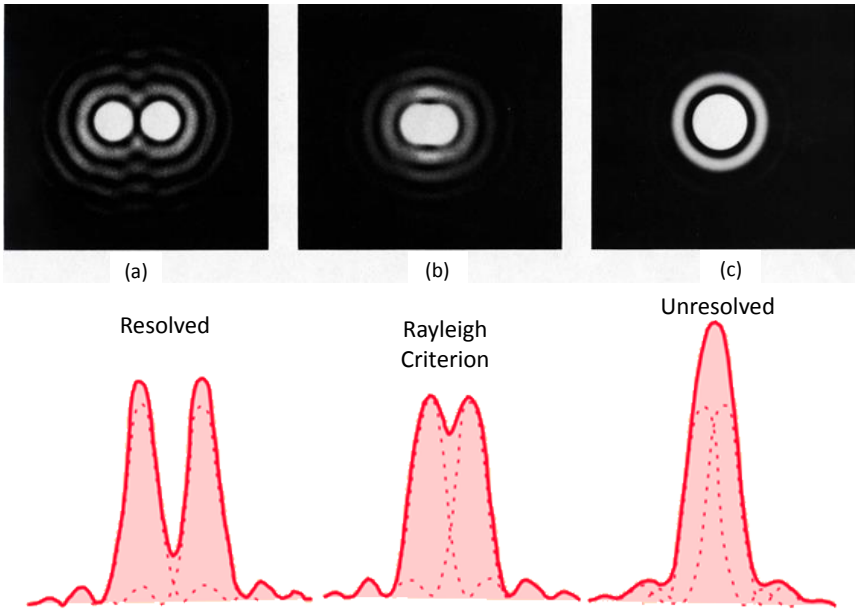

Figure 2.13: The first image shows distant sources, well-resolved. The second, two close image just resolved and the last shows an unresolved image [20].

Chapter 3

Experiments and results

In this chapter, we will present the measurements that were done with our setup to optically characterize and manipulate the spin states of NV^-. We begin by describing our setup. Then we discuss the method for preparing of the nanodiamond samples including the calibration method of our optical system. In the last two sections we will show the results of the detection of single particles; and the spin states manipulation via the ODMR technique in the absence and presence of an external magnetic field. Finally, Rabi oscillations experiments allow us to obtain information about the relaxation time (T_2^*) of the spin state. To start, we will describe the details of the apparatus that allowed us to do our research.

3.1 Experimental setup

The experimental setup (scheme shown in Figure 3.1) was built to implement the principles of confocal microscopy technique, mentioned in section 2.1, that allows us obtain images with high spatial resolution. This is important because we are interested in investigating the light coming from a nanodiamond with a single NV defect. On the optical table we use a linearly polarized solid-state CW laser source (Shanghai Laser & Optics Century, GL532T3-200) emitting at 532 nm. The output beam passes through an acousto-optic modulator (AOM) (Isomet, model 1205C-2), which works as a switch to generate fast optical pulses. This AOM is excited by pulses generated via a pulse pattern generator

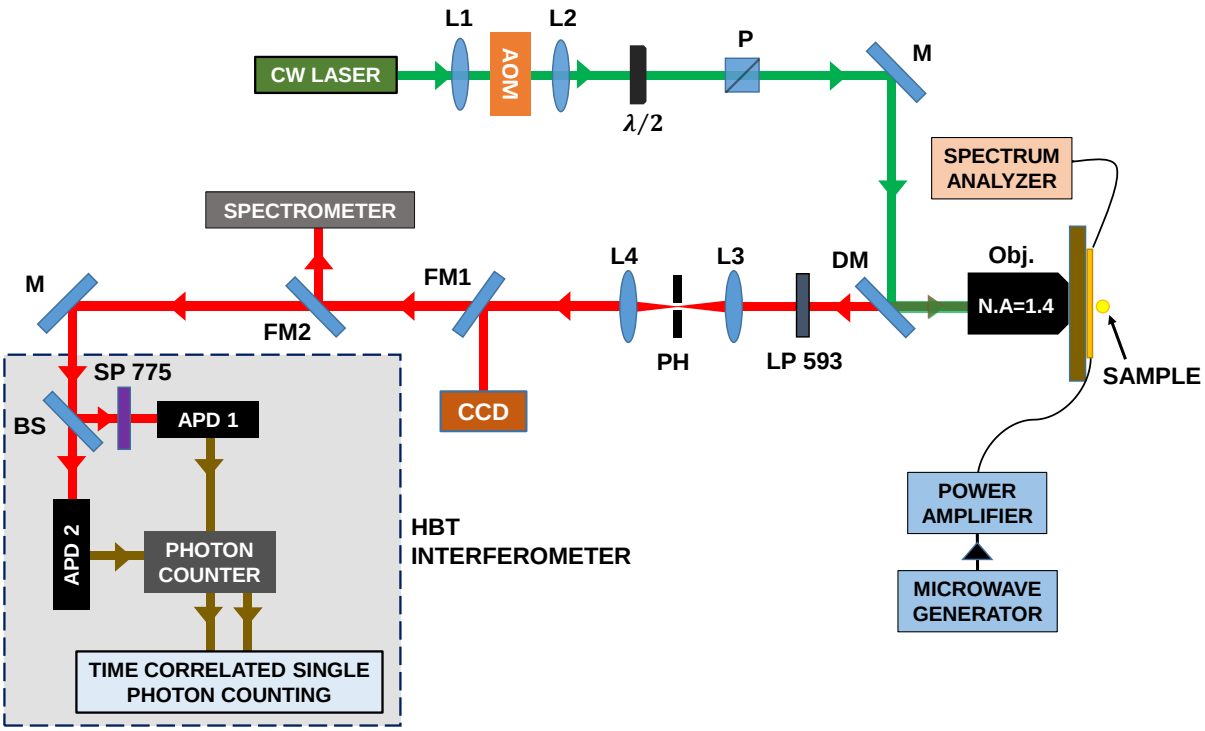

Figure 3.1: Diagram of the optical setup. The CW laser ($\lambda = 532$ nm) is focused through an acousto-optic modulator (AOM). Then both the half waveplate $\lambda/2$ and the polarizer (P) are used to control the power of the laser delivered to the microscope. Light is reflected by a dichroic mirror (DM) to a high N.A. objective (Obj) which focuses light onto a single nanoparticle and collects part of its fluorescence. The fluorescence can be to sent to a high sensitive CCD camera by flipping a mirror (FM1) to obtain an image. It can also be sent by another flip mirror (FM2) to a spectrometer to get a fluorescence spectrum or even sent to a HBT interferometer to obtain a correlation function making use of Time Correlated Single Photon Counting (TCSPC).

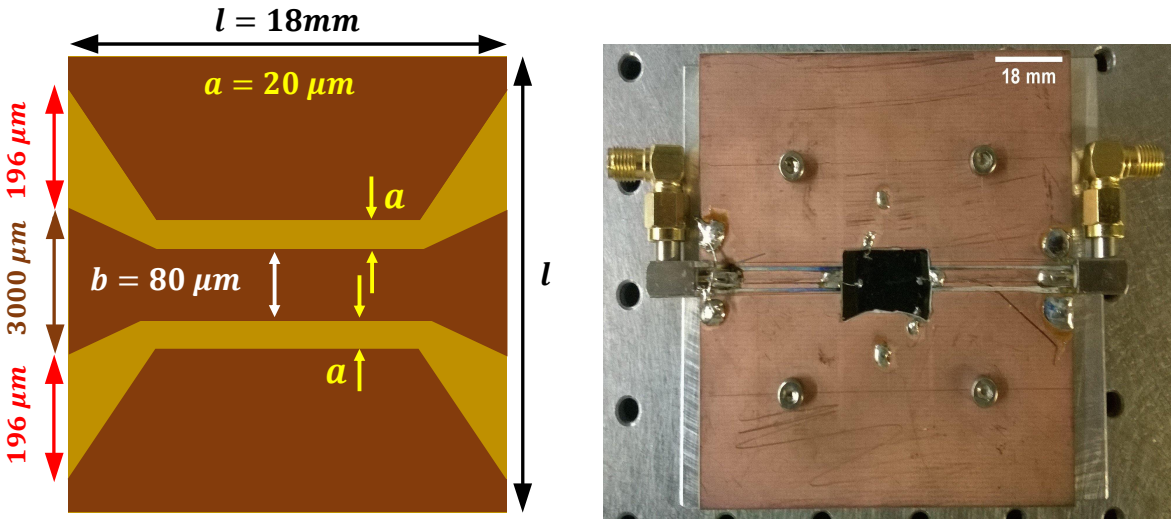

(a) (b)

Figure 3.2: (a) Scheme of the antenna used in the experiment (the dimensions are not to scale). The antenna was designed using lithography to pattern a photoresist on a coverslip. (b) Antenna holder with the antenna in the center. This is used to facilitate the placement of the antenna over the piezo stage. Two SMA connectors are welded on the holder for in-and out coupling the microwave field used to perform Optically Detected Magnetic Resonance (ODMR).

card (SpinCore Technology, Pulse Blaster ESR-PRO 500). Light that passes through the AOM hits on the surface of a dichroic mirror (which reflects green light and transmits red light). The reflected light with the maximum power of 300 μW is driven towards an objective lens of high numerical aperture (Olympus, UPlanSapo 100X/1.4 oil), that makes part of an inverted optical confocal microscope. This resulted in an intensity of $\sim$ 470 kW/cm^2 at the objective focus (see section 3.2.2). Light is focused on the surface of a coverslip on which a microwave antenna was deposited by lithographic methods [42]. The coverslip with the antenna (Figure 3.2) is placed on a holder made from Rogers board and then on a 2D piezoelectric actuator (Piezosystem Jena 88510) fed by homemade low-noise ($1 : 10^5$) high power amplifiers, that moves the holder in the xy plane allowing us to do scans over a determined region of the antenna. The fluorescence light that is collected in reverse through the same objective is sent back toward the dichroic mirror that filters part of the excitation light and allows the fluorescence to pass. We use a 593 nm Long Pass (LP) filter (Semrock, FF01-593/LP) to further eliminate residual light from the ex-

citation beam. Following the principles of the confocal microscopy we use two lenses and a pinhole; lens L3 (100 mm) of Figure 3.1 serves to focus the fluorescence light towards a pinhole (PH) with an aperture of 25 μm. The PH is used as a spatial filter that blocks light coming from perifocal regions allowing us to obtain higher resolution images. In the output the light diverges, so we use the lens L4 (100 mm) to collimate the beam and do not lose the signal that is going to form the images. These optical images are produced by fluorescence being emitted from the scanned region where the particles were deposited by spin coating and can be seen using a single-photon sensitive CCD camera (Hamamatsu ORCA-ER-1394, C4742-80-12AG). Additionally, a spectrometer (Princeton Instruments, SP2500i) with a single-photon sensitive CCD camera (Andor Technology, DU401A-BV) are used to make fluorescence spectra (Figure 2.10b) of the nanodiamond defects, at room temperature.

In the experiment it is very important to know whether the particle being observed is a single emitter. For that, we built an optical system known as HBT interferometer. That interferometer gives us the possibility of measuring the second-order correlation function of the emitted fluorescence which allows us to indicate whether one deals with a single emitter. In a simple description, the HBT interferometer (see Figure 3.1) consists of a 50:50 beamsplitter which sends light to two avalanche photodiodes (APD), that are the detectors situated at two outports of the beamsplitter. When a photon impinges over the APD1, it not only triggers an electron avalanche but also emits infrared (IR) light, in a phenomenon known as cross-talk [43]. The emitted IR photons can influence the single-photon detection events creating a fake signal in other neighboring APD (APD2), thereby creating additional spurious photon correlation events. To avoid that, we placed a 775 Short Pass (SP) (Semrock, FF01-775/SP) in front of the APD1.

3.2 Samples and preparation

In this section we discuss on the characteristics of the nanodiamonds sample and of the cleaning method that we use to remove the organic residues from the antenna where will deposit the nanodiamonds.

3.2.1 Nanoparticles and microwave antenna

The nanodiamond particles (Microdiamant AG, quantum particles QP25) that we use in our experiments have an average a size of 25 nm containing zero, one or two NV^- defects. An antenna (Figure 3.2a) was designed using photolithography to pattern a photoresist on a coverslip. Then one sputtered 5 nm of chromium, 180 nm of gold and 5 nm of chromium again. Nanodiamonds and the antenna were provided by the Nano Optics Group of the Humboldt university of Berlin, Germany.

Nanodiamonds are deposited on the surface of the antenna and it is very important that it is clean. So, we adopted a cleaning method with piranha solution. This is a mixture of concentrated sulfuric acid (70%) with hydrogen peroxide (30%) in a ratio of 4:1. This solution must be prepared in a glass beaker because the reaction produced is highly exothermic, so we must be very careful when placing the antennas inside the beaker. The antennas have to be placed immediately after making the solution to profit from the reaction. Fifteen minutes are enough for remove the organic impurities. Then the antennas must be rinsed during approximately 3 minutes, three times in three different beakers with deionized water to ensure a good cleaning and finally dried with a nitrogen jet.

The process of deposition of nanoparticles on the antennas is done in our lab by means of the spin coating technique, which uses a centrifugal force to produce a homogeneous distribution of nanodiamonds on the surface of the antenna. The nanodiamonds come in a suspension of ignored concentration. 10 μl of this suspension are taken with a micropipette after a sonication process, which consist in placing our sample inside a ultrasonic bath during 15 minutes approximately. After that a puddle of the sample with nanodiamond

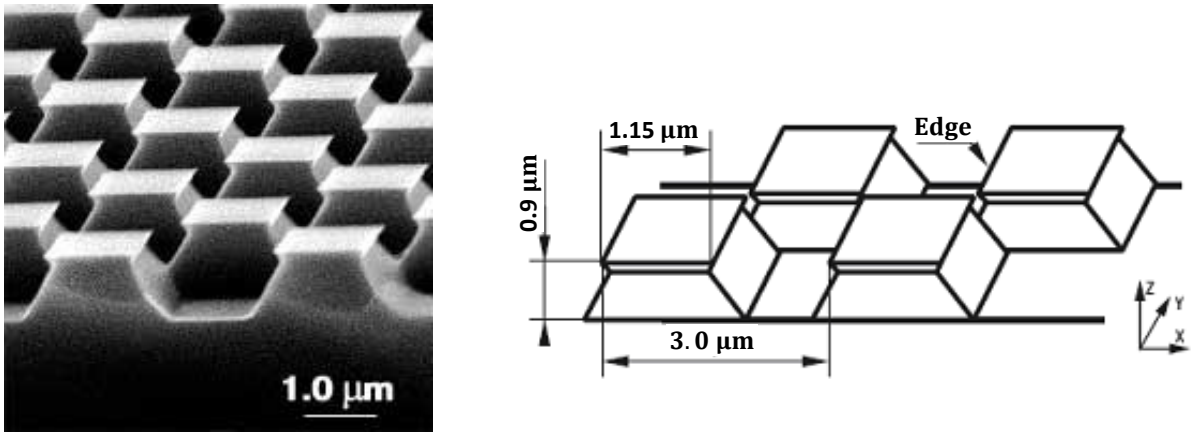

Figure 3.3: (a) Scanning electron microscope (SEM) image of the calibration grating. (b) Dimensions of the grating [41].

particles is dropped in the center of the antenna and is spread over its surface using a spin coater (Chemat Technology inc., KW-4A). We set up the first spining cycle to ramp for 6 seconds until 1500 rpm and the second spinning cycle at 2800 rpm for 15 seconds. After that, the sample should be ready to be used. Since cleaning process of the antenna is very important, every step explained above must be done carefully. Otherwise organic material could land on the antenna surface, which can be critical and lead to a blinking phenomenon that makes impossible the photostability and detection of the fluorescence signal coming from the region where the single nanodiamond is placed.

3.2.2 Optical confocal microscope calibration

Before beginning the experiment with diamond samples we have to characterize our optical system and to measure its spatial resolution. In order to do that, first we calibrate the optical system using a calibration grating (NT-MDT company, Test grating TGX1) which has a period of 3000 nm. The Figure 3.3a shows a SEM image of the grating and Figure3.3b its dimensions. With this grating we will find the relation of equivalence between pixels and nanometers in our CCD camera. Figure 3.4a shows an image of the grating after being illuminated with laser light. The brilliant/dark points are consequence of the constructive/destructive interference given by the optical path difference between

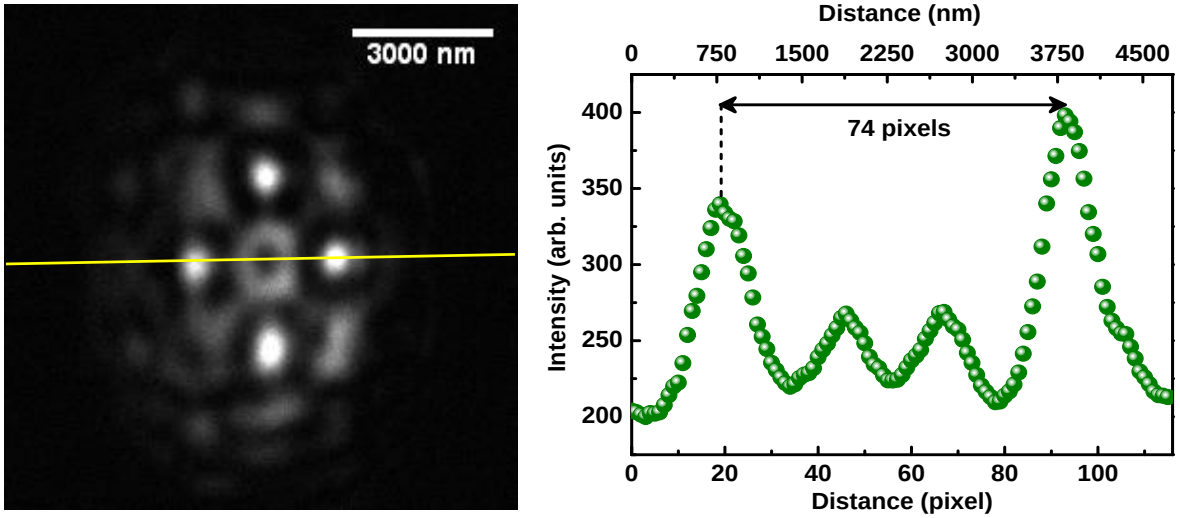

(a) (b)

Figure 3.4: (a) Image of a test grating used to calibrate the optical system. (b) Intensity profile obtained when making a cross section of (a).

the upper and lower surfaces. Making a cross section we obtained an intensity graphic 3.4b. The peak to peak distance is 74 pixels that should be equal to the period of the grating. Thus

$$\frac{3000\ nm}{74\ pixels} \approx 41 \frac{nm}{pixel} \tag{3.1}$$

So far, we made the calibration of our system. Now, taking into account this result we can to do a measure of the PSF of the system to know the resolution of the system. To do that use dye doped beads with 20 nm in diameter because they are particles easier to detect since they emit stronger fluorescence than the nanodiamonds with a central wavelength at 610 nm. The method used for the preparation of this calibration sample is the same that we describe above but in this case the deposition was on simple coverslips. Figure 3.5a shows a fluorescence image of an individual bead where the yellow line is traced to obtain a cross section. This gives us a fluorescence profile which FWHM, according to section 2.4, is the PSF of the optical system. In this case the FWHM $\approx$ 7 pixels. Using the relation 3.1, we find that FWHM $\approx$ 287 nm. This means that each particle with size less than 287 nm will be seen by the system as having a size of 287 nm. Theoretically,

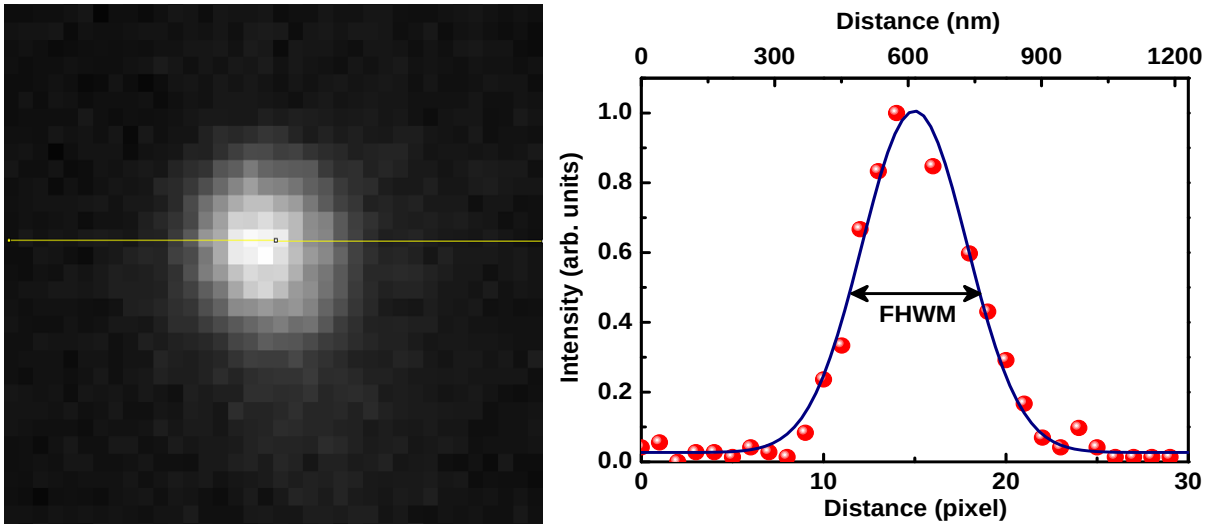

(a) (b)

Figure 3.5: (a) Image of a particle of 20 nm used to measure the PSF of our system. (b) Intensity profile where the FWHM gives us the PSF.

using the Equation 2.64 we obtain d = 244 nm. The differences between the two measures could be because the pinhole that we are using is not adequate and leaves to passes light from the perifocal regions.

With this characterization of our optical system, we are able to move on and in next section we will detect single defect particles.

3.3 Detection of single NV$^-$ defects in nanodiamonds

One way of determining if the observed particle has embedded NV$^-$ defects is via fluorescence spectroscopy. The typical fluorescence spectrum of nanodiamonds with NV$^-$ defects is known and can be obtained using a spectrometer coupled to a sensitive CCD camera. Figure 2.10b shows a characteristic spectrum that was measured in our lab at room temperature. In spite of giving us information if the illuminated diamond contains NV$^-$ defects it is not possible to know a priori if the nanodiamond has only one defect embedded in it. If we want to know this we should measure the second-order correlation function of the light emitted by the single nanodiamond.

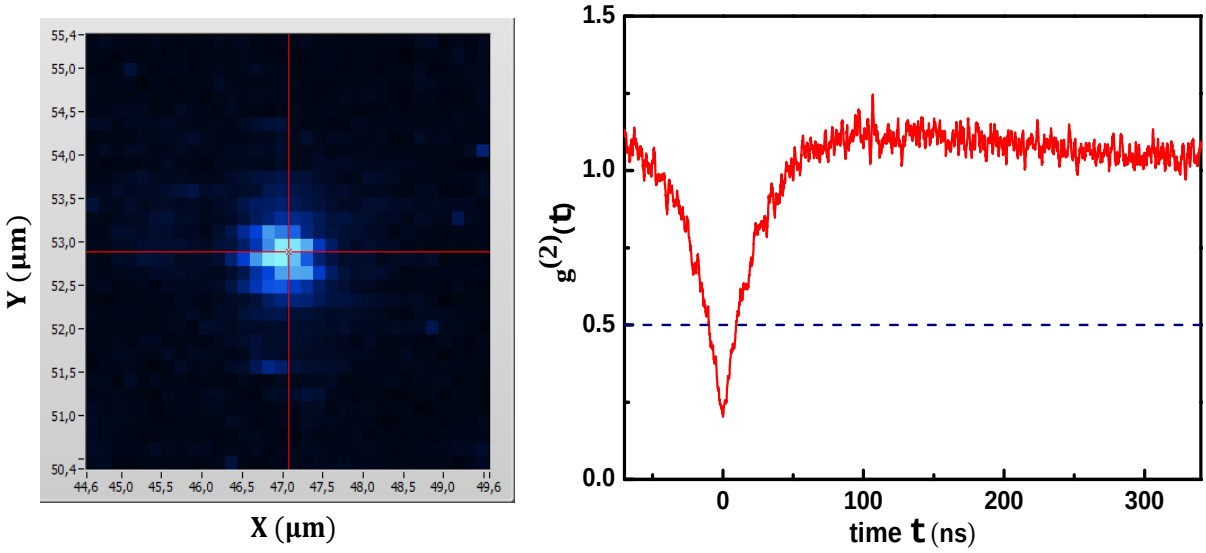

(a) (b)

Figure 3.6: (a) Scanning fluorescence image over an antenna region showing that nanodiamonds are being detected. (b) Second-order correlation function of the nanoparticles fluorescence. Here we get $g^{(2)} < 0.5$, which guarantees that we have a single photon emitter.

In order to find a single nanodiamond we realize a scan over a micrometric region (typical: 10 μm $\times$ 10 μm) using a xy-piezo scanner. The confocal image (Figure 3.6a) is a product of the light coming from the illuminated region in the antenna. In a typical image it is easy to observe bright points which may correspond to NV$^-$ defects. We investigate them one by one and measured the second-order correlation function $g^{(2)}(\tau)$ to observe if it is antibunched, corresponding to a single emitter. The fluorescence coming from the illuminated region is focused on two APDs connected each one to two home made photon counters. These counters show us in a display the number of photons (typically 4×10^4 counts/s in the linear regime of the excitation) detected by the APDs in a given time window (in our case 100 ms) and furthermore re-transmit this signal to a time correlated single photon counting (TCSPC) module (PicoQuant, Time Harp 200).

The sequence in the detection process is as follows: when a photon is detected by the APD1 the time counter of the TCSPC module starts counting the time until a photon is detected by a APD2. All this is considered as an event. The difference in time between

the first and second detected photons (photons detected by APD1 an APD2, respectively) is the information sent via electrical signals to the TCSPC module. The number of events detected versus the delay time τ when each event is detected are represented in histogram that is proportional to the $g^{(2)}(\tau)$ function. If the histogram presents a dip such that $g^{(2)}(0) < 1$ we are seeing a characteristic quantum behavior of light (Figure 3.6b). In the last chapter Equation 2.26 is used to characterize individual emitters. If $g^{(2)}(0) < 0.5$, we have detected a nanodiamond with a single defect. The fact that the dip doesn't go to zero is due to the noise of the system generated by detection of non fluorescence light that arrives to the APDs and also by their dark counts.

From now on, all results shown in this dissertation are obtained with particles containing single NV$^-$ defects.

3.4 Spin state manipulation of single NV$^-$ defect in nanodiamonds

NV defects in diamond, in particular NV$^-$ defects, present a known spin system that can be polarized via optical excitation as well as coherently manipulated by a microwave and optically read out. In this section, we discuss on a technique known as Optically Detected Magnetic Resonance (ODMR), an important tool that gives us the possibility of manipulating the electronic spin states in single NV$^-$ defects and study their dynamics in the presence and absence of an external magnetic field. By means of the application of microwave pulse sequences one is able, for example, to observe Rabi oscillations.

3.4.1 Optically Detected Magnetic Resonance

After verifying that the nanodiamond with NV$^-$ defect is a source of single photons (so one deals with a single defect) we can implement a protocol to coherently manipulate its spin states using microwave fields from by a microwave generator (Aim & Thurlby Thandar Instruments TGR6000) and a pulse generator card (SpinCore Technology, Pulse Blaster ESR-PRO 500) in combination with a LabView card. The Pulse Blaster is a

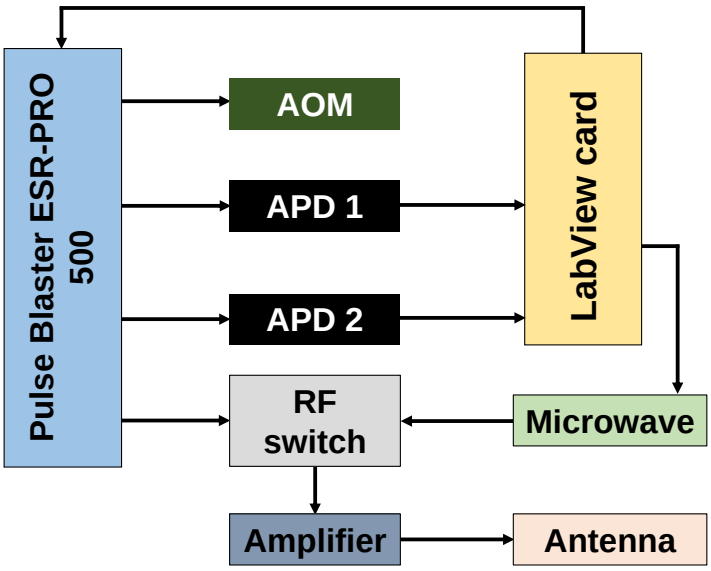

Figure 3.7: Simplified diagram showing the electronic architecture used to realize the ODMR experiment. We use a LabView card to control the system. Via an interface we can control the pulse generating plate (ESR-PRO 500) and the microwave generator. Furthermore, the LabView interface does the readout of the fluorescence from the diamonds from APD1 and APD2.

versatile, high-performance pulse/pattern TTL signal generator that operates at speeds of up to 500 MHz and generates pulses ranging from 2 ns to 8.59 s per instruction at intervals ranging from 10 ns to 9 s per instruction. Figure 3.7 is a diagram that shows the part of the experimental setup used to generate pulse sequences.

The pulse blaster card has four channels that are controlled by a LabView routine. The first channel sends TTL pulses towards the AOM that works as a switch to control the on/off state of the CW laser. Channels two and three are connected to LabView and allow the readout of the APDs 1 and 2 respectively. Channel four is used to control the microwave system. A RF switch (Mini-Ciruits ZASW-2-50DR+) controls the on/off state of the microwave signal that will be amplified (Mini-circuits ZHL-16W-43-S+) by 45 dB and then sent towards the antenna containing the nanodiamonds.

The system described above allows the manipulation of the NV⁻ spin states, inducing transitions between Zeeman levels of the electronic ground state, leading to population

inversion which dynamics is explained by the optical Bloch equations described in the last chapter. Here we drive both optical and microwave transitions in a sequential way. As mentioned in section 2.3, due to the structure of the electronic states it is possible to optically initialize the system, manipulate and read out the NV^- spin state. The system initialization in diamonds with NV^- defects consists in leaving the system in its lower energy state $m_s = 0$ (Figure 2.10a) via optical pumping [44]. The optical transition is spin-preserving, but also occurs that the electron in the $m_s^* = \pm 1$ state has higher probability to non-radiatively decay to a metastable singlet state [45] with a lifetime of 250 ns [28] aproximately. After it relaxes to the $m_s = 0$ ground state. With this selective process we are polarizing the system into $m_s = 0$. The part of the manipulation occurs when we drive spin flips towards the degenerated $m_s = \pm 1$ using a microwave field. Thus, we can find the transition frequency between the $m_s = 0$ and $m_s = \pm 1$ by sweeping the microwave frequency while the readout is done by monitoring the fluorescence coming out of the nanopaticle. In the following we use this technique to observe the fluorescence behavior for different values of microwave power and its behavior when the diamond is in presence of an external magnetic field.

3.4.2 NV^- spin state transitions

In the absence of external magnetic fields, the above described procedure can be realized if we make the following sequence of pulses (Figure 3.8a). First, we initialize the spin states with a excitation beam laser in ON state all the time while the APD1 (Reference-REF) is collecting, during 200 μs, the fluorescence coming from the sample that will be used to do the normalization of the signal (for example, to eliminate fluctuations of excitation laser power). Then, a microwave pulse with a frequency 2.800 GHz and lasting 200 μs is turned on with a fixed frequency while the APD2 (Signal-SIG) realizes the collection of the fluorescence at the same time. That pulse sequence is repeated once again after increasing the microwave frequency by typically 750 kHz. When the microwave frequency approached 2.870 GHz we note a drop in the detected fluorescence with a contrast of 14%, as shown in the Figure 3.8b. This measure is in agreement with results found in

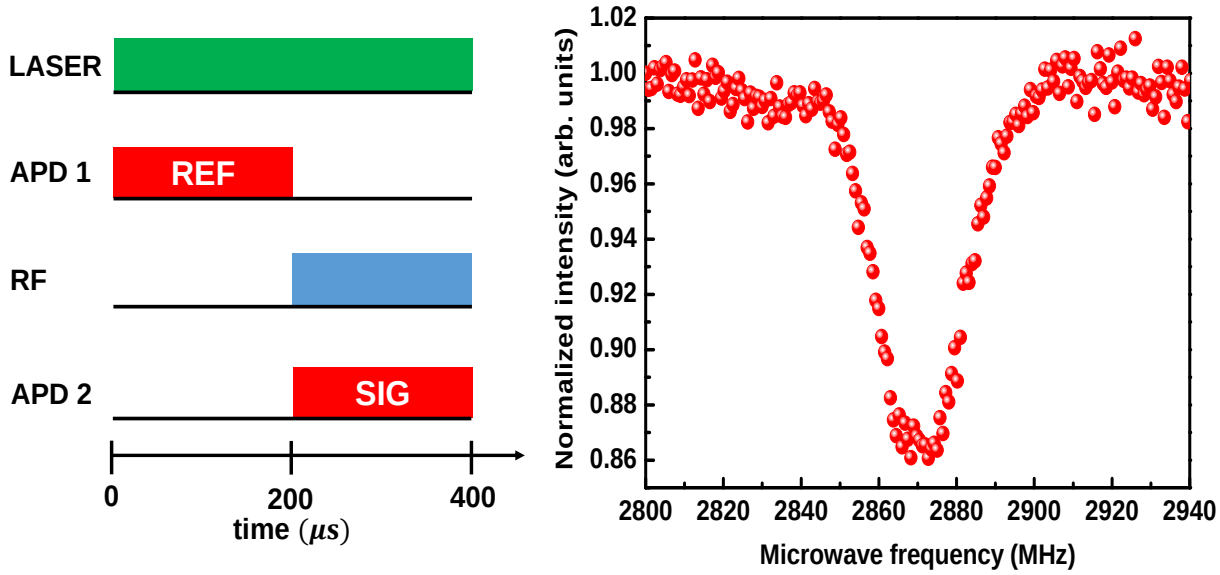

(a) (b)

Figure 3.8: (a) Scheme of the pulse sequence used in ODMR. (b) ODMR signal in zero external magnetic field. The dip is centered at the typical frequency of 2870 MHz.

other works [28,46] that were realized at room temperature. In [28] a contrast of 30% was obtained while in [46] only 10% contrast was measured. These different results depend on the coupling between the electric field and the moment dipole and branching ratios between the $m_s = 0$ and $m_s = \pm 1$ into and out of the singlet system [47].

In the next experiment we take into account the effects of the microwave power. It was possible to observe the power broadening phenomenon [46] by means of the ODMR spectrum: we can find the linewidth of the spin-flip transition by measuring the FHWM of the ODMR. In chapter 2, we do refer to two mechanisms able to cause linewidth broadening: i) Radiation broadening due to the spontaneous emission that appears after the interaction with a light field and produces a natural linewidth of 2γ. ii) An electric/magnetic field interacting with the system also produces a linewidth broadening mechanism given in Equation 2.53.

In Figure 3.9a we show ODMR spectra for different microwave powers. The ODMR spectrum with low contrast corresponds to a low microwave power. In Figure 3.9b we

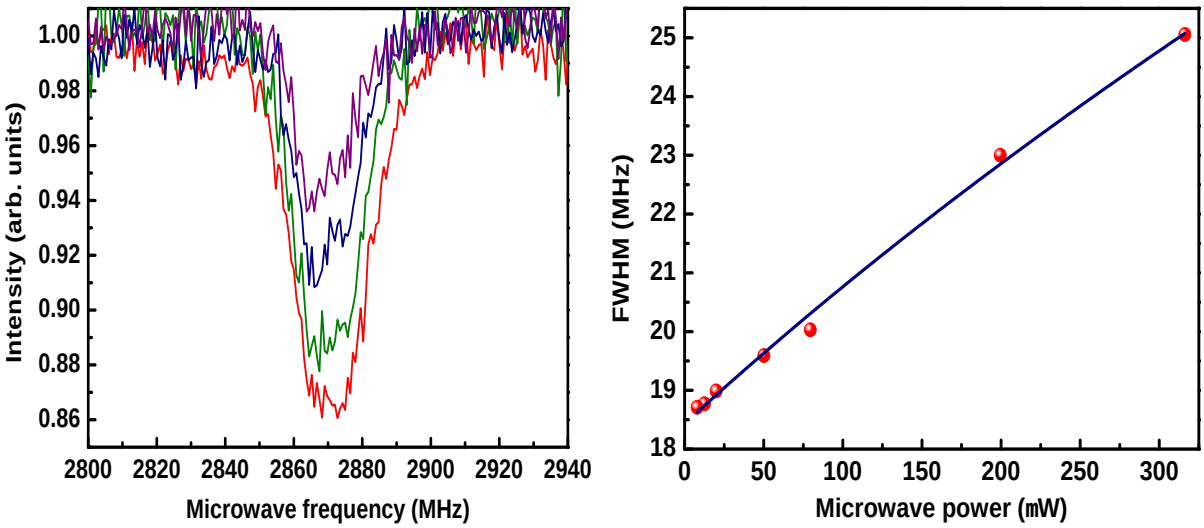

(a) (b)

Figure 3.9: (a) ODMR spectrum experimenting power broadening due to changes in microwave power from the purple curve until red curve with 50, 79, 200 and 316 μW, respectively. (b) Linewidth for different microwave powers. The point close to zero power is the narrowest linewidth, measured by the FWHM, found in our experiments.

made a fit by using of Equation 2.53 and introducing the Rabi frequency in terms of microwave power (see Equation 3.5). Thus we rewrite Equation 2.53 as

$$2(\gamma^2 + \frac{1}{2}(\alpha\sqrt{P})^2)^{1/2} \tag{3.2}$$

When we do the fit, we leave α and γ as free parameters. The values obtained for each one are: $\gamma = 9.2$ MHz in agreement with the literature [28] and $\alpha = 0.7\sqrt{J.s}^{-1}$ that is the coupling parameter between $\bar{\mu}$ and $\bar{E}$, point which will be discussed later. When trying to make further measurements with microwave powers smaller than 8 μW the noise effects become more notorious and is difficult to measure a magnetic resonance curve. We extrapolated the experimental data of the Figure 3.9b to find a possible natural linewidth. That extrapolation give us as result approximately 18.4 MHz while in the literature is typically 10 MHz. This difference could be due the influences of the CW lase as is discuss on pages 52-53.

Effect of an external magnetic field

In presence of an external magnetic field we can lift the degeneracy of the $m_s = \pm 1$ levels by means of the Zeeman effect as shown in Figure 3.10a. The splitting $\Delta\omega$ between the levels $m_s = -1$ and $m_s = +1$ is directly proportional to the magnetic field as the relation $\Delta\omega = 2\gamma' B_z$ where $\gamma' = 2\pi \times 28$ GHz/T is the electron gyromagnetic ratio and B_z is the magnetic field along the quantization axis, defined along the line passing by the nitrogen atom and the vacancy in the nanodiamond lattice [28].

The ODMR spectrum in this case will be different, appearing two dips due to the two different resonance frequencies: the first one between $m_s = 0$ and $m_s = -1$ and the second one between $m_s = 0$ and $m_s = +1$. Figure 3.10b shows the experimental setup built to observe the Zeeman effect. One sees the antenna illuminated from below by the excitation laser; above it, a permanent magnet (NdFeB) was attached to a micrometric positioner that allows the movement of the magnet in three directions. In this experiment, we transversely positioned the magnet right above the nanodiamond under observation and we only move the magnet in the direction perpendicular to the antenna's plane.

The ODMR spectrum obtained after bringing the magnet in the neighborhood of the nanodiamond is shown in the Figure 3.10c. The ODMR spectrum is now affected by the magnetic field and shows two dips at two different frequencies due to the splitting caused by Zeeman effect. This fact can be used to realize coherent manipulation of the spinstate in a independent way between the $m_s = 0$ and $m_s = -1$ and $m_s = 0$ and $m_s = +1$ sublevels, depending on the microwave frequency that we choose to drive the transitions [48]. We can notice the direct dependence that exists between the Zeeman split and the intensity of the magnetic field as is evidenced in a frequency shift (Δf) due to variations in the intensity of the external magnetic field (see Figure 3.10d). Thus, when the magnet is away from the nanodiamond, we say that we have a low magnetic field, obtaining a small splitting, but as the magnet is approached to the nanoparticle we have a high magnetic field and the splitting increases. That splitting carries information about the magnetic field parallel to the NV^- axis. Devices that measure magnetic fields with NV^- defects use the above described effect because this reflects the direct relation with

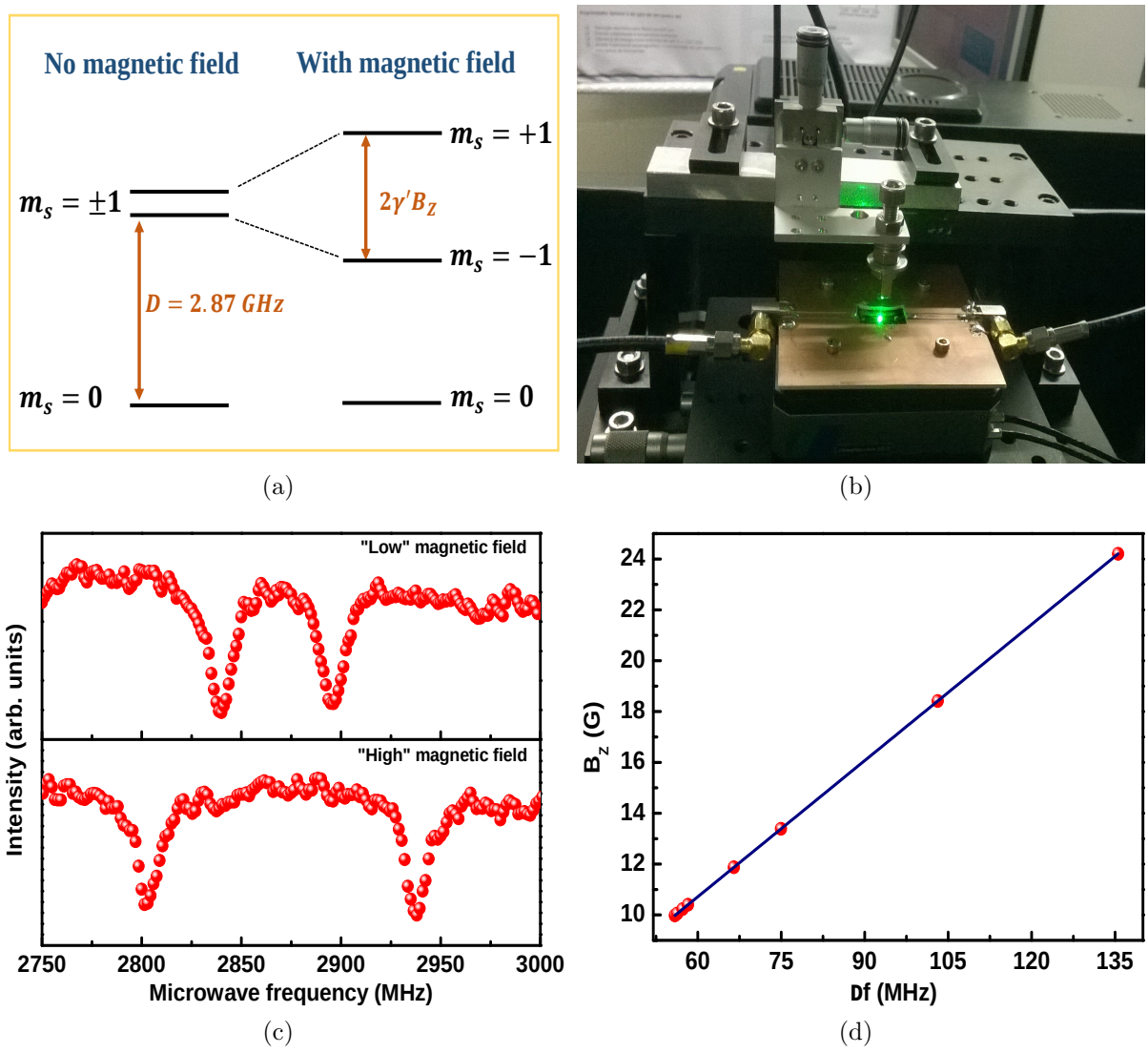

Figure 3.10: (a) Levels' scheme of the ground state showing the split of the $m_s = \pm 1$ sublevels in the presence of an external magnetic field. (b) Experimental setup built with a micrometric positioner and a small rectangular magnet. We can manually control the magnet position in three directions. (c) ODMR spectrum when an external magnetic field is applied. Here we note that the split is greater when we have a stronger magnetic field. "Low" or "High" magnetic field means that we are bringing the magnet away or close to the antenna. (d) Measurement of Zeeman field B_z versus a shift (Δf) in frequency due to the presence of the external magnetic field generated by a permanent magnet.

the magnetic field projection along the direction of the NV^- defect quantization axis [49]. So, the ODMR technique can be used to probe magnetic fields because the shift in the resonance frequency is proportional to external magnetic field [50, 51]. Furthermore, due of its small size in the nanometric scale, nanodiamonds can ensure proximity of the NV^- defect to the sample. Maintaining a short distance we can be able to realize nanoscale magnetic image by scanning the NV^- defect with respect to the sample and monitoring its fluorescence [52].

3.4.3 Rabi oscillations in the ground sate

The possibility of polarizing the spin of the NV^- defect and inducing transitions via microwave frequency between the $m_s = 0$ and $m_s = \pm 1$ electronic ground state allows us realize coherent manipulation between the spin states of the electron. The simplest experiment is to observe Rabi oscillations. That kind of oscillations are known as Rabi oscillations and they are obtained following a known protocol based in the Ramsey method [25].

The implementation of a pulse sequence (Figure 3.11) is done between the $m_s = 0$ and $m_s = \pm 1$ sublevels of the ground sate. We work with a fixed frequency which was found in the ODMR experiment to be 2.870 GHz. The microwave pulse sequence in this Rabi oscillations, like for the ODMR experiments, was carried out with the Pulse Blaster card. With this pulse sequence we can find that the characteristic oscillatory behavior is product of the coherent drive of the transitions in the spin two-level system in the electronic ground state. When the area of the microwave pulses is equal to a multiple of π we invert completely the population of the spin states in the electronic ground state. This type of pulse is known as π pulse and accordingly to equations 2.39 and 2.40 is dependent on the microwave power and on the duration of the microwave pulse [26]. In the experiment, we keep the microwave power constant (316 μW) and vary the time duration of the microwave pulses from 0 to 1500 ns. Then, we obtain the population oscillations between the spin states that shows oscillations of the fluorescence emitted by single NV^- defect. The protocol in this sequence is the following: First, the system is

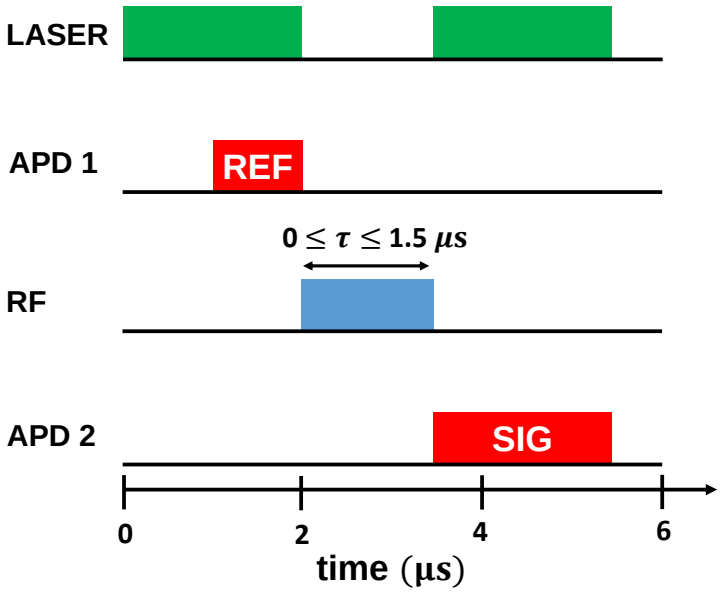

Figure 3.11: Pulse sequence implemented to do coherent manipulation of transitions between the spin states $m_s = 0$ and $m_s = \pm 1$ in the electronic ground state.

optically polarized via optical pumping for 2 μs such that the spin of the system state is the $m_s = 0$ state. The APD 1 ("reference" used to normalize the spectrum) is ON during the last microsecond. Then, while the laser is blocked, spin flip transitions are generated by the microwaves (frequency set in 2.870 GHz) between the $m_s = 0$ and $m_s = \pm 1$ states. To end the sequence, the laser is turn on again at the same time that the APD 2 is detecting fluorescence. This sequence is done several times incrementing the length of the microwave pulse in steps of 10 ns. Figure 3.12a shows the Rabi oscillations for one nanodiamond with a single NV$^-$ defect. We can do a theroretical fit using the following Equation [54]

$$\rho_{ee}(t) = s \cdot \left\{ 1 - c \cdot \frac{\Omega^2/2}{2\gamma^{*2} + \Omega^2} \left[1 - \left(cos\lambda^* t + \frac{3\gamma^*}{2\lambda^*} sin\lambda^* t \right) e^{-\frac{3\gamma^* t}{2}} \right] \right\} \tag{3.3}$$

where $\lambda^* = (\Omega^2 - \gamma^{*2}/4)^{1/2}$ and $\gamma^* = 1/T_2^*$. In the experiment, s is the maximum value obtained by the fluorescence (at time $t = 0$) and c is the contrast between the states. With this scheme, knowing the Rabi frequency we can obtain the decoherence time T_2^*. To do that, we extract the damping term of the Equation 3.4 and use it to make the fitting. It is the expression to fit the dampened (D_{damp}) curve

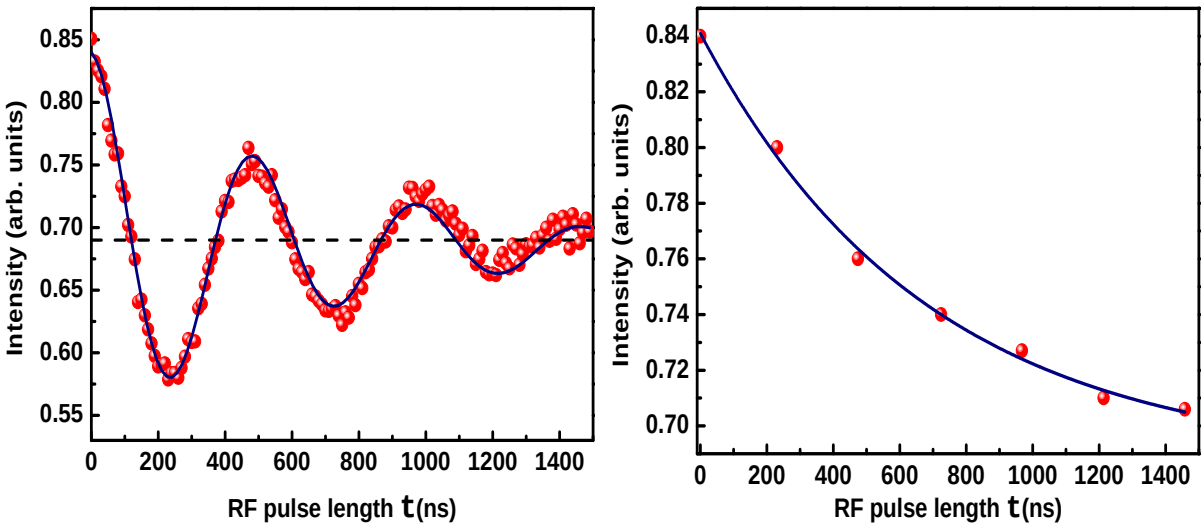

(a) (b)

Figure 3.12: (a) Experimental Rabi oscillations (red points) and theoretical fit (blue curve). The microwave power used was of 316 μW. (b) Experimental data (red points) extracted from the Rabi oscillations data. The curve is very well fitted to the experimental points in according to the Equation 3.4. We obtain $T_2^* \approx 1\mu s$.

$$D_{damp} = s \cdot c \cdot \frac{\Omega^2/2}{2\gamma^{*2}\Omega^2} e^{-\frac{3\gamma^* t}{2}} \tag{3.4}$$

Figure 3.12a clearly shows a damping in the oscillations due to the exponential term given in the Equation 3.3. So, we can fit an exponential decay curve with the maximum values obtained by the oscillation. Furthermore, we also take advantage of the symmetry of the oscillations for getting more experimental points to the experimental decay fit. For that we draw a symmetrical horizontal line that serves for reflecting, like a mirror, the minimum values and for increasing the number of points that allows a better fit. We can see that the Figure 3.12b is fitted according to an exponential curve given by the Equation 3.4. This method gives information about γ^* which inverse is the known as dephasing time (T_2^*) [26]. The value of γ^* is approximately 1 MHz leading to $T_2^* \approx 1\mu s$. These results were obtained with the same nanodiamond for which the ODMR power broadening data were measured (Figure 3.10). This is in contrast to the result of 18.4 MHz obtained in the power broadening experiment. But we have to consider that there we had the green laser on during the whole experiment, so that any coherent created between the spin levels of

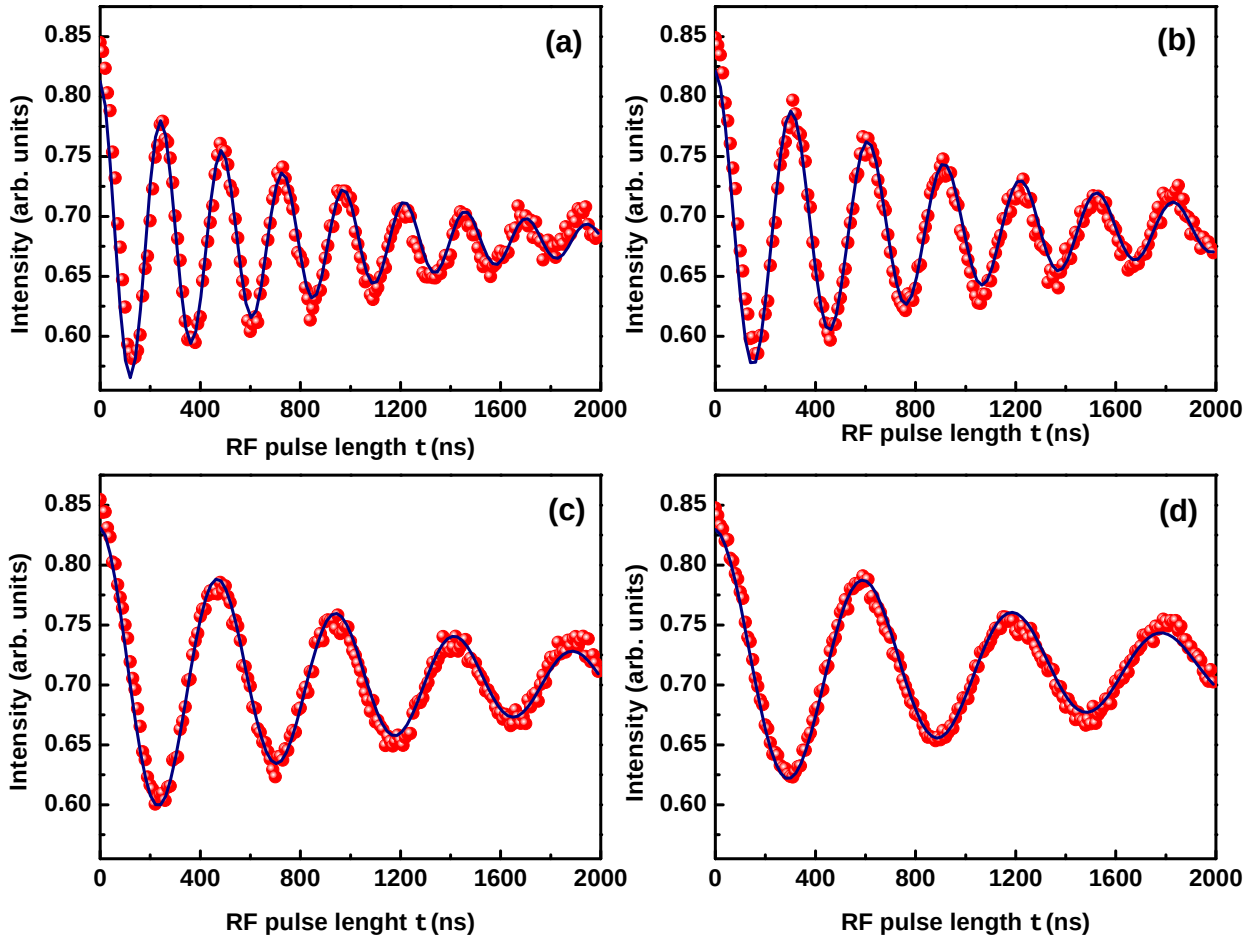

Figure 3.13: Experimental Rabi oscillations (red points) taken at different microwave powers and their corresponding fits (blue curve). The power decreases from (a) to (d). Thus, (a) has $\Omega = 25$ MHz, (b) $\Omega = 20$ MHz, (c) $\Omega = 13$ MHz and (d) $\Omega = 10$ MHz each one with microwave powers of 200 μW, 126 μW, 50 μW and 32 μW respectively.

the electronic ground state by the microwave field will be immediately destroyed by the CW laser at 532 nm. Thus, the measurements of the power broadening experiment using a different pulse sequence in order to get rid of these effects.

Figure 3.13 shows the behavior of the Rabi oscillations with the microwave power. We can see that as the microwave power decreases, the time to drive the transitions increases, as expected from the expression $\Omega = \pi/\tau$ for the Rabi frequency. Increasing the power, the populations exchange of the ground state sublevels is faster. The frequency of the Rabi oscillations is proportional to the square root of the microwave power [55]. In Figure

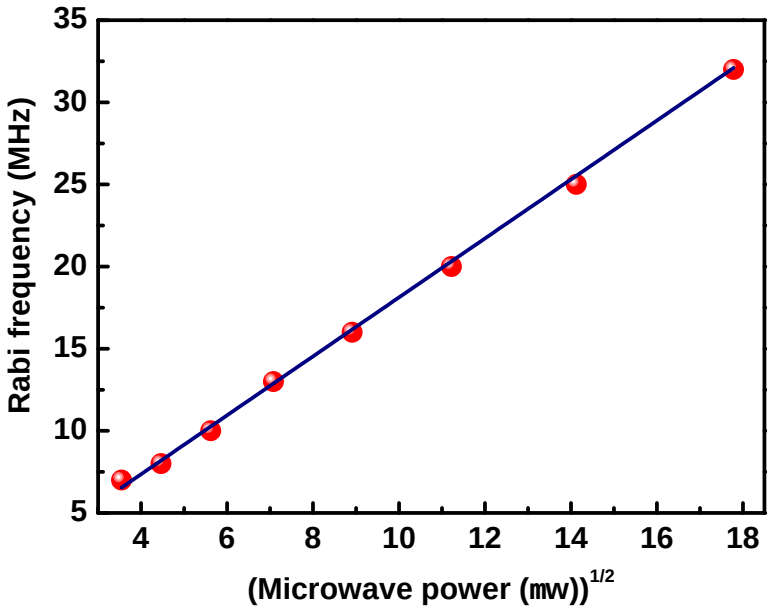

Figure 3.14: Experimental data (red points) of the Rabi frequency taken at different microwave powers. The behavior corresponds to a square root fit (blue curve).

3.14 we make a graph of the measured Rabi frequency for different microwave powers confirming this dependence. The mathematical expression can be written as

$$\Omega = \alpha\sqrt{P} \tag{3.5}$$

where α is the angular coefficient of the straight line in a $\Omega \times \sqrt{P}$ graph that gives us information about the coupling of the $\vec{\mu}$ with $\vec{E}$. This coefficient is specified for each nanodiamond. The last experiment was done in one single nanodiamond and the angular coefficient found was of $\alpha = 1.7\sqrt{J \cdot s}^{-1}$. We know that

$$\Omega = \frac{|\bar{\mu}||\bar{E}|}{\hbar}\cos\theta \tag{3.6}$$

and

$$P \propto |\bar{E}|^2. \tag{3.7}$$

Then, we can define b as a proportionality constant, so we have

$$P = b^2|\bar{E}|^2 \Longrightarrow |\bar{E}| = \frac{\sqrt{P}}{b} \tag{3.8}$$

replacing the last equation in 3.6, we obtain

$$\Omega = \frac{|\bar{\mu}|cos\theta}{b\hbar}\sqrt{P} \tag{3.9}$$

Now, comparing with 3.5 find that

$$\alpha\hbar = \frac{|\bar{\mu}|cos\theta}{b} \tag{3.10}$$

with the last expression just knowing the b parameter we would obtain information about the projection of the dipolar momentum on the magnetic field vector. That is, we can find out the angle between $\bar{\mu}$ and $\bar{E}$. Unfortunately, we haven't had time to carry out these measurements and making the correspondent analysis any further.

Chapter 4

Conclusions and perspectives

In this work, we have learned new techniques which were implemented in our laboratory with the finality to study intrinsic properties of individual particles of nanoscopic size, in particular nanodiamonds. Following the principles of confocal microscopy, the optical microscopy system was calibrated. The relation camera pixels/nanometers was of 41 nm/pixel. The measured point spread function of the optical system is of approximately 287 nm which is comparable to the resolution d = 232 nm given by the Rayleigh criterion. We can thus say that in our microscope any particle smaller than this value will be seen by the optical system as having a size of 287 nm.

The single NV^- defect in nanodiamond showed to be a photostable single photon source that can be detected via second-order correlation function. The value found for $g^2(0)$ was of 0.2 which proves single photon emission since $0 < g^2(0) < 0.5$. Thus, we can say that the particle investigated is a nanodiamond with a single defect and that it is a single photon emitter source.

Using Optically Detected Magnetic Resonance we measured a resonance frequency for the paramagnetic triplet ground state of 2.870 GHz which is in agreement with what is found in the literature. The same kind of measurements was realized for different microwave powers in order to find a possible natural linewidth. The value found, after extrapolating the experimental data, was approximately 18.4 MHz while in the literature this is found to be typically in the range of 10 MHz [28, 56].

Another property shown by the single NV^- defects is their sensitivity to an external magnetic field without losing its photoluminiscence properties at room temperature. We find changes in the the Zeeman field felt by the nanodiamond corresponding to a few Gauss which is in agreement with data in literature [56].

Finally, we drove radio frequency transitions between the $m_s = 0$ and $m_s = \pm 1$ states to generate Rabi oscillations in experiments aiming to measure the coherence time due to inhomogeneities of the local environment. We have find $T_2^* \approx 1\ \mu s$, corresponding to a linewidth of ≈ 1 MHz. This is in contrast to the result of 18.4 MHz obtained in the power broadening experiment. However, we remark that during these experiments the excitation laser is on all the time. The electronic transitions to the excited state promoted by the laser destroys the coherence induced between the spin states of the electronic ground state, leading to a broader spin flip resonance linewidth.

In the near future we intend to realize a coherent control of a single spin using the spin-echo technique in order to measure local magnetic fields, where in this time a minimal resolved field is in the order of the nanoteslas [50]. The spin-echo technique consists in a pulse sequence where first a $\pi/2$ pulse in t=0 creates a spin state of maximum coherence. Then, due to local magnetic inhomogeneities, the net moment precesses during a time τ and the signal decays. A π pulse refocuses the dephasing induced by static and slowly varying magnetic fields; the final state is therefore reached regardless of the actual magnetic field value, as long as the phase shifts induced in both halves of the free evolution time are the same. Thus, the spin echo is insensitive to static fields and fluctuations on a time scale longer than the sequence length (see Figure 4.1). The echo amplitude decays on a time scale referred as coherence time T_2. Since T_2^* describes decoherence induced by noise over the full frequency range and T_2 only for higher frequency noise, one has $T_2 > T_2^*$. With this technique, we can obtain coherence T_2 time of several microseconds and in this way increase the sensitivity to measure magnetic field [56].

Also, we intend to implement a nanomagnetometer to monitor and eventually stabilize a current that passes by a microwire. To do that we will use a microwave bias-tee which

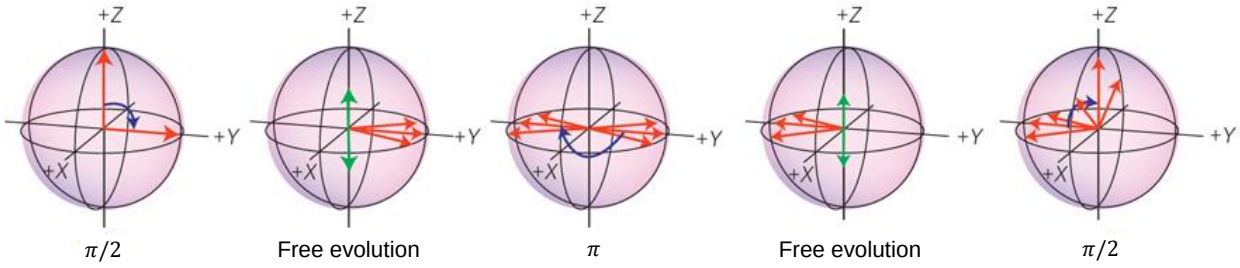

Figure 4.1: A $\pi/2$ pulse is first applied to the spin system making the dipole rotates down into the X'Y' plane. The dipole begins to dephase in a free evolution. Then a π pulse is applied. This pulse rotates the dipole by π about the X' axis. The π pulse causes a rephasing of the dipole to produce a signal called an echo. Finally, a $\pi/2$ pulse returns to the dipole to its initial state.

allows us send current and microwave through the same antenna. Thus, we will have a current that generates a magnetic field when passing through of the microwire, which will be detected by our nanodiamond under the influence of the microwave field sent via the bias-tee. The magnetic field generated for a current passing through the microwire is known to be

$$B = \frac{\mu_0 I}{2\pi r} \tag{4.1}$$

then,

$$I = \frac{2\pi r}{\mu_0} B. \tag{4.2}$$

The magnetic field and the distance of the nanodiamond to the wire's center can be measured, the rest of the equation is constant, so measure the current is supposed not to be a problem.

References

[1] W. G. Breiland *et al.* "Optically detected electron spin echoes and free precession in molecular excited states". Phys. Rev. Lett. **30**, 158 (1973).

[2] Tycko R. *et al.* "Electronic states in gallium-arsenide quantum-wells probed by optically pumped NMR". Science **268**, 1460 (1995).

[3] B. E. Kane "A silicon-based nuclear spin quantum computer". Nature **393**, 133 (1998).

[4] F. Jelezko and J. Wrachtrup. "Single defect center in diamond: A review." Phys. Stat. Sol. (a) **203**, 3207 (2006).

[5] M. Geiselmann *et al.* "Fast optical modulation of the fluorescence from a single nitrogen–vacancy centre". Nature Physics **9**, 785 (2013).

[6] J. Wrachtrup and F. Jelezko "Processing quantum information in diamond". J. Phys.: Condens. Matter **18**, 807 (2006).

[7] A. Dréau *et al.* "Avoiding power broadening in optically detected magnetic resonance of single NV defects for enhanced dc magnetic field sensitivity". Phys. Rev. B **84**, 195204 (2011).

[8] Y. Mita "Change of absorption spectra in type-Ib diamond with heavy neutron irradiation". Phys. Rev. B **53**, 360 (1996).

[9] J. Wolters *et al.* "Enhancement of the zero phonon line emission from a single nitrogen vacancy center in a nanodiamond via coupling to a photonic crystal cavity". Appl. Phys. Lett. **97**, 141108 (2010).

[10] M. W. Doherty *et al.* "Electronic Properties and Metrology Applications of the Diamond NV^- Center under Pressure". Phys. Rev. Lett. **112**, 047601 (2014).

[11] L. Rodin *et al.* "Magnetometry with nitrogen-vacancy defects in diamond". Rep. Prog. Phys. **77**, 056503 (2014).

[12] G. Kucsko *et al.* "Nanometre-scale thermometry in a living cell". Nature **500**, 54 (2013).

[13] I. Aharonovich *et al.* "Diamond photonics". Nature Phot. **5**, 397 (2011).

[14] P. Maletinsky *et al.* "A robust scanning diamond sensor for nanoscale imaging with single nitrogen-vacancy centres". Nature Nanotechnology **7**, 320 (2012).

[15] R. Hanbury-Brown and Twiss "Correlation between photons in two coherent beams of light". Nature **177**, 27 (1956).

[16] R. Hanbury-Brown and Twiss "A test of a new type of stellar interferometer on Sirius". Nature **178**, 1046 (1956).

[17] C. Emary *et al.* " Bunching and antibunching in electronic transport". Phys. Rev. B **85**, 165417 (2012).

[18] E. Hecht . Optics. 4th ed. Pearson Education, 2002.

[19] M. Fox. Quantum Optics: An introduction. 1st ed. Oxford University Press, 2006.

[20] http://hyperphysics.phy-astr.gsu.edu/ April 11, 2016.

[21] R. Loudon. The Quantum Theory of Light. 2nd ed. Oxford Science Publications; Oxford University Press, 1983.

[22] M. O. Scully and Zubairy, Quantum Optics. 1st ed. Cambridge University Press, 1997.

[23] D. F Walls, G. J. Milburn. Quantum Optics. Springer Velag, 1994.

[24] A. Batalov *et al.* "Temporal Coherence of Photons Emitted by Single Nitrogen-Vacancy Defect Centers in Diamond Using Optical Rabi-Oscillations". Phys. Rev. Lett. **100**, 077401 (2008).

[25] G. Gilbert, A. Aspect. Introduction to Quantum Optics: From the semi-Classical Aproach to Quantized Light. Cambridge University Press, 2010.

[26] L. Allen and J. H. Eberly. Optical Resonance and Two-Level Atoms. John Wiley & Sons, Inc. 1975.

[27] N. Mizuochi *et al.* "Electrically driven single-photon source at room temperature in diamond". Nature Photon **6**, 299 (2012).

[28] R. Schirhagl *et al.* "Nitrogen-Vacancy centers in diamond: nanoscale sensors for physics and biology". Annu. Rev. Phys. Chem. **18**, 83 (2014).

[29] M. W. Doherty *et al.* "The nitrogen-vacancy color centre in diamond". Phys. Rep. **528**, 1 (2013).

[30] F. Jelezko *et al.* "Single spin states in a defect center resolved by optical spectroscopy". Appl. Phys. Lett. **81**, 2160 (2002).

[31] A. Lenef *et al.* "Electronic structure of the $N-V$ center in diamond: Experiments". Phys. Rev. B **53**, 427 (1996).

[32] N. B. Manson *et al.* "Nitrogen vacancy center in diamond: Model of the electronic structure and associated dynamics". Phys. Rev. B **74**, 104303 (2006).

[33] J. H. N Loubser and J. A. Van Wyk, "Electron spin resonance in the study of diamond". Rep. Prog. Phys. **41**, 1201 (1978).

[34] L. J. Rogers *et al.* "Infrared emission of the NV centre in diamond: Zeeman and uniaxial stress studies". New J. Phys. **10**, 103024 (2008).

[35] G. Balasubramanian *et al.* "Nanoscale imaging magnetometry with diamond spins under ambient conditions". Nature **455**, 648 (2008).

[36] P. Newmann *et al.* "Excited-state spectroscopy of single NV defects in diamond using optically detected magnetic resonance". New J. Phys. **11**, 013017 (2009).

[37] J. Wrachtrup and F. Jelezko, "Processing quantum information in diamond". J. Phys.: Condens. Matter **18**, S807 (2006).

[38] J. G. White *et al.* "An evaluation of confocal versus conventional imaging of biological structures by fluorescence light microscopy". J. Cell Biol. **105**, 41 (1987).

[39] M. Minsky "Memoir on inventing the confocal scanning microscope". Scanning **10**, 128 (1988).

[40] R. Corle and S. Kino. Confocal Scanning Optical and Related Imaging Systems. Academic Press, 1996.

[41] NT-MDT (Molecular Devises and Tools for Nanotechnology), www.ntmdt.com, March 29, 2012.

[42] S. M. Palhade and S. P. Yawale "Design and photo-lithographic fabrication of microstrip patch antenna". Int. J. Sci. Res. **4**, 2319 (2015).

[43] D. A. Kalashnikov *et al.* "Accessing photon bunching with a photon number resolving multi-pixel detector". Optics Express **19**, 9352 (2011).

[44] S. Choi *et al.* "Mechanism for optical initialization of spin in NV^- center in diamond". Phys. Rev. B **86**, 041202 (2012).

[45] M. W. Doherty *et al.* "The negatively charged nitrogen-vacancy centre in diamond: the electronic solution". New J. Phys. **13**, 025019 (2011).

[46] A. Gruber *et al.* "Scanning Confocal Optical Microscopy and Magnetic Resonance on Single Defect Centers". Science **276**, 2012 (1997).

[47] E. Oliver. "Development of a Diamond-based Scanning Probe Spin Sensor Operating at Low Temperature in Ultra High Vacuum". Ph. D. Thesis. Institute of Physics, University of Stuttgart (2014).

[48] R. Hanson *et al.* "Room-temperature manipulation and decoherence of a single spin in diamond". Phys. Rev. B **74**, 161203 (2006).

[49] J. R. Maze *et al.* " Nanoscale magnetic sensing with an individual electronic spin in diamond". Nature **455**, 644 (2008).

[50] S. Hong *et al.* " Nanoscale magnetometry with NV centers in diamond". Materials Research Society **38**, 155 (2013).

[51] H. J. Mamin *et al.*" Nanoscale nuclear magnetic resonance with a nitrogen-vacancy spin Sensor". Science **339**, 557 (2013).

[52] S. Steinert *et al.* "High sensitivity magnetic imaging using an array of spins in diamond". Rev. Sci. Instrum. **81**, 043705 (2010).

[53] B. Kwasi "Optical and spin properties of nitrogen vacancy centers in bulk and nanocrystalline diamond". Masters Dissertation. Massachusetts Institute of Technology (2013).

[54] B. Sontheimer. "Optical and spin coherence properties of nitrogen vacancy center in nanodiamond". Master Dissertation. Humboldt University of Berlin (2014).

[55] J. J. Pla *et al.* "A single-atom electron spin qubit in silicon". Nature **489**, 541 (2012).

[56] C. L. Degen "Scanning magnetic field microscope with a diamond single-spin sensor". Appl. Phys. Lett. **92**, 243111 (2008).